

# Analysis of Equibiaxial Tension Tests for Hyperelastic EAP Film

huan lu (✉ [luoha@njcit.cn](mailto:luoha@njcit.cn))

Nanjing College of Information Technology <https://orcid.org/0000-0001-6744-4050>

Yin-Long Zhu

Nanjing Forest Police College

Hai-Feng Zhao

Nanjing College of Information Technology

Jing-Jing Zhang

Nanjing College of Information Technology

---

## Original Article

**Keywords:** Hyper elasticity, Equibiaxial tension test, EAP, Bulge test, Radial tension, Equibiaxial planar tension

**Posted Date:** April 9th, 2021

**DOI:** <https://doi.org/10.21203/rs.3.rs-402426/v1>

**License:** © ⓘ This work is licensed under a Creative Commons Attribution 4.0 International License.

[Read Full License](#)

---

## Title page

**Hua-An Luo**, born in 1968, is currently an associate professor at *Nanjing Vocational College of Information Technology, China*. He received his PhD degree from *Nanjing University of Aeronautics and Astronautics, China*, in 2015. His research interests include mechatronics engineering, intelligent material, flexible actuator.

Tel: +86-25-85842324; E-mail: luoha@njcit.cn

**Yin-Long Zhu**, born in 1981, is currently an associate professor at *Nanjing Forestry University, China*. He received his PhD degree from *Nanjing University of Aeronautics and Astronautics, China*, in 2012. His research interests include mechatronics engineering, intelligent material, flexible robot.

Tel: +86-25-85427751; E-mail: ylzhu@njfu.edu.cn

**Hai-Feng Zhao**, born in 1981, is currently an associate professor at *Nanjing Vocational College of Information Technology, China*. He received his PhD degree from *North University of China, China*, in 2020. His research interests include intelligent material, sensor design.

Tel: +86-25-85842176; E-mail: zhaohf@njcit.cn

**Jing-Jing Zhang**, born in 1979, is currently a lecturer at *Nanjing Vocational College of Information Technology, China*. He received her master degree from *Chongqing University of Posts and Telecommunications, China*, in 2005. Her research interests include electromechanical engineering and hydraulic technology.

Tel: +86-25-85842324; E-mail: zhangjj@njcit.cn

Corresponding author: Hua-An Luo E-mail: luoha@njcit.cn

## ORIGINAL ARTICLE

# Analysis of Equibiaxial Tension Tests for Hyperelastic EAP Film

Hua-An Luo<sup>1</sup> • Yin-Long Zhu<sup>2</sup> • Hai-Feng Zhao<sup>1</sup> • Jing-Jing Zhang<sup>1</sup>

Received March xx, 2021; revised April xx, 2021; accepted March xx, 201x

© Chinese Mechanical Engineering Society and Springer-Verlag Berlin Heidelberg 2021

**Abstract:** Equibiaxial tension tests for hyperelastic electroactive polymers (EAPs) are important means to obtain the mechanical properties. There are three main methods: equibiaxial planar tension, radial tension and bulge test. The finite element analysis software is used to model and analyze the influence of testing apparatus, specimen geometric parameters on the test results and accuracy. The results show that the uniformity of the deformation of the square film can be effectively improved by using single corner point fixed tension in equibiaxial planar tension test, and the force error also decreased; the number of the cuts and the size of punched holes should be appropriate in radial tension test of circular diaphragm specimen to avoid the material strength failure caused by excessive tension along the edge of transition arc between grips and excessive deformation of tensile belt between the cuts; in bulge test, the sampled deformation data should be near the spherical pole to obtain more accurate stress-strain relationship owing to contour error and non-uniform deformation, a certain range of model parameters will limit the scope of simulation analysis. This paper proposed research provides guidance for the design of equibiaxial tension test apparatus and method to obtain more accurate test results.

**Keywords:** Hyper elasticity • Equibiaxial tension test • EAP • Bulge test • Radial tension • Equibiaxial planar tension

## 1 Introduction

Recently, equibiaxial testing of rubber-like materials is becoming prevalent for establishing the mechanical properties of the hyperelastic film [1–4]. Because there exists obvious discrepant between uniaxial tension and biaxial tension test results, and the friction between contact

surfaces during uniaxial compression makes it have complex stress states such as compression and shear, which makes the actual test results inaccurate. Therefore, the equibiaxial tension test of hyperelastic film is an indispensable means to determine the mechanical properties. There are three typical equibiaxial tension test methods, i.e. equibiaxial planar tension test for square specimen, radial tension test for circular specimen and bulge test for inflating circular specimen (Figure 1).

After the pioneer works about the rabbit skin test finished by Lanir and Fung in 1974 [5], the equibiaxial planar tension test has been widely used in the mechanical property studies of soft tissue materials [6]. The strain of such materials is small, at the same time the specimens generally need to be processed. Another common application field of the equibiaxial tension is polymer materials such as rubbers [7–9] with the characteristic of hyperelasticity. In these cases, the non-uniform deformation near the corner in the tension test will affect the accuracy of the test results [10]. Yutaka obata [11] modified the corner chucks to minimize non-uniformity of the deformation of the specimen at the corners; Blatz et al. added clamps at four corner points of square film specimen for clamping and stretching [12]; Jacobs used finite element software to analyze the stress concentration and stress shielding problems in biaxial planar tension [13]. Due to the fact that the equibiaxial planar tension equipment can meet the requirements of uniaxial, biaxial and equibiaxial tension tests, the most testing machines were developed for equibiaxial planar tension. However, there are also deficiencies in the complex structure and large size of such machines. Then a special radial tension mechanism

✉ Hua-An Luo  
luoha@njcit.cn

<sup>1</sup> School of Intelligent manufacturing, Nanjing Vocational College of Information Technology, Nanjing 210023, China

<sup>2</sup> College of Mechatronics Engineering, Nanjing Forestry University, Nanjing 210037, China

appeared for equibiaxial tension test [4, 14], the specimen is made of cut circular sheet.

Inspired by the phenomenon that the inflated balloon expands into a sphere with equibiaxial deformation, the bulge test was used for equibiaxial tension test at the earliest. By modeling the rubber film, Treloar [15] explored the shape and strain distribution on the sphere surface with inflated in varying degrees. Rivlin and Saunders [16] adopted the data acquired from the pole region of the inflated diaphragm as the uniform two-dimensional tensile

data of the strain energy potential of Yeoh. Adkins and Rivlin [17] firstly used the Neo-Hookean and Mooney form of strain energy to conduct meaningful theoretical research. Hart Smith [18] used exponential hyperbolic model to further analyze the bulge test and verify the previous research results. The bulge test apparatus is simple in structure and easy to operate, making it the first choice for equibiaxial tension test such as EAP membrane materials [9, 19].

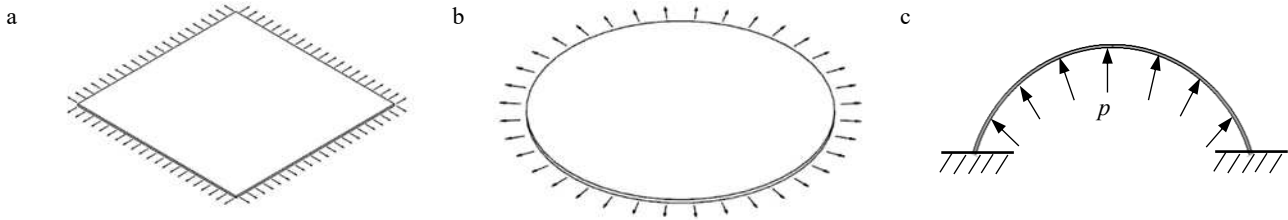


**Figure 1** Typical equibiaxial tension test: (a) Equibiaxial planar tension, (b) Radial tension and (c) Bulge test

VHB acrylic series hyperelastic EAP elastomers are provided by 3M™ with characteristics of large elasticity and high strain energy density, possessing a wide application prospect in hightech fields such as soft robot [20], actuator [21], flexible sensor [22–23] and other dielectric elastomer transducers [24–25]. In this paper, the stress-strain relationship of hyperelastic EAP film under quasi-static condition was studied. The finite element analysis software ABAQUS was used to simulate the three typical equibiaxial tension tests and analyze their characteristics. The accuracy of the methods was compared, and the influence of typical test apparatus structure and specimen geometry parameters on the accuracy were also discussed. The conclusion of this paper is helpful for the selection and application of equibiaxial tension test method and the design of the device.

## 2 Constitutive Model of Hyperelastic Film Materials Based on Equibiaxial Tension

For hyperelastic rubber-like materials, it is considered that the energy (work) stored in the materials depends only on the initial and final state of deformation, which is independent of the path of deformation (or load). Therefore, the most convenient way to describe the stress-strain constitutive relation of such hyperelastic materials is by means of strain energy potential. The commonly used strain energy potentials are as follows.

### 2.1 Mooney-Rivlin Model

For incompressible materials, the strain energy potentials can also be considered as a function of two strain invariants

[26–27]:

$$W = \sum_{k+l=N} C_{kl} (I_1 - 3)^k (I_2 - 3)^l \quad (1)$$

where  $C_{kl}$  are Mooney-Rivlin material parameters,  $N$  is model order. In practical application, the first two terms of its power series are usually taken, i.e.

$$W = C_{10}(I_1 - 3) + C_{01}(I_2 - 3) \quad (2)$$

here  $I_1$  and  $I_2$  are the strain invariants of Cauchy-Green deformation tensor, determined by the stretch ratios  $\lambda_i$  ( $i=1, 2$  and  $3$ ) in three principal directions, and the stretch ratio is the ratio of the specimen length after stretching to the original one in principal directions:

$$I_1 = \lambda_1^2 + \lambda_2^2 + \lambda_3^2 \quad (3)$$

$$I_2 = \lambda_1^2 \lambda_2^2 + \lambda_2^2 \lambda_3^2 + \lambda_3^2 \lambda_1^2 \quad (4)$$

### 2.2 Yeoh Model

In the strain energy potential formula of Mooney-Rivlin, if only term  $I_1$  is partially expanded, the typical third order Yeoh strain energy potential can be obtained [28]:

$$W = C_{10}(I_1 - 3) + C_{20}(I_1 - 3)^2 + C_{30}(I_1 - 3)^3 \quad (5)$$

### 2.3 Ogden Model

Ogden removed the restriction that the strain energy

potential is an even power of the stretch ratio and proposed a strain energy potential in series form [29]:

$$W = \sum_{k=1}^N \frac{\mu_k}{\alpha_k} (\lambda_1^{\alpha_k} + \lambda_2^{\alpha_k} + \lambda_3^{\alpha_k} - 3) \quad (6)$$

Where  $\mu_k$ ,  $\alpha_k$  are the material parameters. In some literatures [9, 19], the above-mentioned Ogden strain energy potential usually takes another form:

$$W = \sum_{k=1}^N \frac{2\mu_k}{\alpha_k} (\lambda_1^{\alpha_k} + \lambda_2^{\alpha_k} + \lambda_3^{\alpha_k} - 3) \quad (7)$$

This formula is also used in the finite element analysis software ABAQUS. It is basically the same as the original formula with only formal difference. For incompressible materials, with the relation  $\lambda_1\lambda_2\lambda_3=1$ , the strain energy potential can be simplified.

#### 2.4 Stress-Strain Relationship Based on Equibiaxial Tension

According to the strain energy potential, the principal Cauchy stress  $\sigma_i$  ( $i=1, 2$  and  $3$ ) can be derived:

$$\sigma_i = \lambda_i \frac{\partial W}{\partial \lambda_i} - P_h \quad (8)$$

where  $P_h$  is the hydrostatic pressure, which is determined by the dynamic boundary condition. According to  $\sigma_3=0$ , the expressions of the stress in two principal directions under the condition of equibiaxial tension can be deduced:

$$\sigma_1 = \sigma_2 = \sigma = \lambda_1 \frac{\partial W}{\partial \lambda_1} - \lambda_3 \frac{\partial W}{\partial \lambda_3} \quad (9)$$

Under the assumption of isotropy and incompressibility,  $\lambda_1 = \lambda_2 = \lambda$ ,  $\lambda_3 = 1/\lambda^2$ , the equibiaxial tensile stress  $\sigma$  can be derived. When the strain energy potential of Yeoh or Mooney-Rivlin was used, Eq. (9) also can be rewritten directly in terms of  $I_1$  and  $I_2$  as

$$\sigma = 2(\lambda^2 - \lambda^{-4}) \left( \frac{\partial W}{\partial I_1} + \lambda^2 \frac{\partial W}{\partial I_2} \right) \quad (10)$$

Substituting the above-mentioned strain energy potential into Eq. (9) or Eq. (10), the stress formula for different models of equibiaxial tension can be obtained. In general, the relationship between engineering stress  $S$  and stretch ration  $\lambda$  is used to express the stress-strain relationship of hyperelastic materials where  $S$  equals to Cauchy stress (also known as real stress) divided by  $\lambda$ :

$$S = \sigma / \lambda \quad (11)$$

The EAP analyzed in this paper is VHB4910 from 3M™, a commercial double-sided adhesive tape, which belongs to acrylic polymer and is widely used to manufacture flexible actuator due to its good deformation capacity under the action of electric field. Referring to the literature [9], the material model parameters are taken as the values in Table 1 below.

**Table 1** Material model parameters

Second order Ogden (Abaqus form) [9]		Second order Mooney-Rivlin	
$\mu_1$ / KPa	64.7	$C_{01}$ / KPa	21.56
$\alpha_1$ / -	1.39689		
$\mu_2$ / KPa	0.0457	$C_{10}$ / KPa	0.0815
$\alpha_2$ / -	5.8638		

Note: The second order Mooney-Rivlin parameters are obtained by refitting the data from the second order Ogden model.

### 3 Equibiaxial Tension Tests Suitable for Hyperelastic Film

#### 3.1 Equibiaxial Planar Tension Test

Equibiaxial planar tension is a method that applying uniform tensile stress (or displacement) to the periphery of the square film specimen to generate equibiaxial planar strain (or stress) (Figure 1(a)). In practical setup, mechanical clamping is required (Figure 2). In order to reduce stress concentration and stress shielding phenomenon [13], the uniformly distributed multipoint tensile method should be designed, and the clamping area minimized as much as possible. The concentrated loads were applied by the chucks along the four sides of the specimen to conduct equibiaxial free tension, where the tangential displacements of the tensile points were not constrained. Due to the resistance friction exists when the chucks moved, and the tensile point near corner cannot provide enough tension to realize lateral "fast" movement of other points, thus resulting in large strain between the tensile points, so the specimen can easily be torn when the stretch ratio is large enough. Therefore, during the stretching process, two clamping points on the mutually perpendicular edges near the corner were fixed each other [10], as seen in Figure 2(a).

It is simple to calculate the stress and strain of equibiaxial planar tension. Measuring and recording the axial tensile force  $F$ , then divided by the original sectional area  $A_0$  of the square film, the nominal stress  $S$  can be obtained, i.e.

$$S = F/A_0 = F/L_s t_0 \quad (12)$$

where  $L_s$  is the side length of the square film specimen,  $t_0$

the original thickness. According to the manufacturer's instructions, the thickness of VHB4910 film is 1 mm. In the simulation, the axial tensile force  $F$  was calculated by summing the tensile force  $f_n$  of the tensile points ( $n=1, 2, \dots, N_p$ , where  $N_p$  is the total number of tensile points along the side), and the tensile force near the corner was taken from its force component. The strain of equibiaxial planar tension was calculated according to the displacement of the testing marks in Figure 2 in practice.

The main factors affecting the equibiaxial planar tension are the number of tensile points and the chucks arrangement near the corner. Among them, the number of tensile points will impact the deformation uniformity and degree of the film specimen. In the two-corner-point-fixed tension (Figure 2(a)), the two fixed corner points will cause non-uniform excessive deformation in the corner area, resulting in tearing of the specimen and adverse impact on the test accuracy. Therefore, four additional chucks also be added at the corner points in the single-corner-point tension to carry out equibiaxial planar tension [12] (Figure 2(b)), where the concentrated forces (or displacements) were exerted only at the corner points. The influence factors and the improvement effects shall be analyzed and verified by finite element simulation.

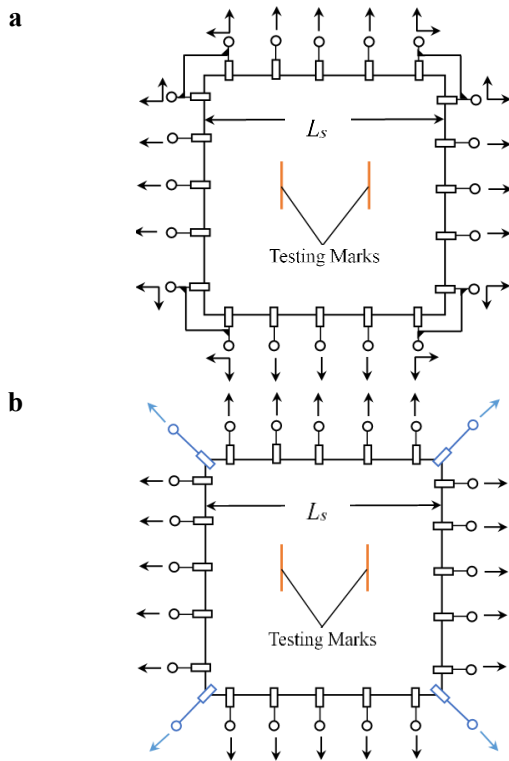


**Figure 2** Equibiaxial planar tension test: (a) two-corner-point-fixed tension and (b) single-corner-point tension

### 3.2 Radial Tension Test

Radial tension test is to apply uniform radial tensile force (or displacement) around the circular diaphragm specimen, so as to obtain the equibiaxial strain (or stress) and get its mechanical properties (Figure 1(b)). Circular film specimen with cuts and punched holes should be used in the actual radial tension (Figure 3) to reduce the tangential forces between the grips. The test apparatus can realize the equibiaxial deformation of the specimen by pulling the cable to move the uniformly distributed grips radially. The actual uniform deformation occurs in the range of the circle ( $\Phi D_i$ ) which externally tangent to the punched holes, and the testing marks in Figure 3 are used for strain measurement during tension test in practice. The nominal stress  $S$  of equibiaxial radial tension is

$$S = F / (\pi * D_i * t_0) \quad (13)$$

where  $F$  is the sum of the radial tensile forces at each grip, and  $t_0$  the original thickness of the film. Generally, the displacement between two testing marks is measured by non-contact optical instrument in practice, then the strain can be calculated.

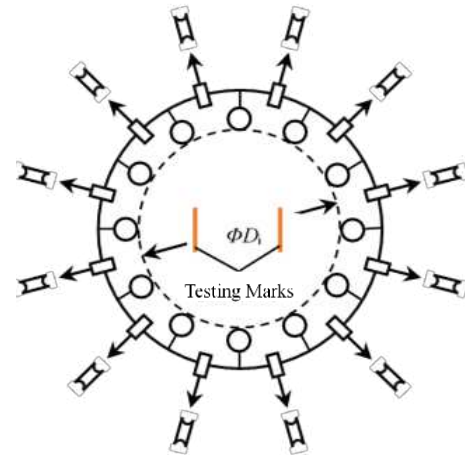


**Figure 3** Radial tension diagram

### 3.3 Bulge Test

In bulge test, the periphery of the elastic disc diaphragm is fixed and hydraulic oil (or compressed air) is applied on the bottom surface to make the film inflated into a sphere (Figure 1). The symmetry of the sphere determines that the equibiaxial stress and strain can be obtained in a natural way. In practice, a test apparatus generally uses upper and lower flanges to place and fix the periphery of the disc diaphragm. While inflating, the elastic film passes through the hole of the upper flange until it looks like a "sphere" shape (Figure

4). The stress-strain relationship can be calculated according to the deformation of inflated balloon and the pressure of hydraulic oil (or compressed air).

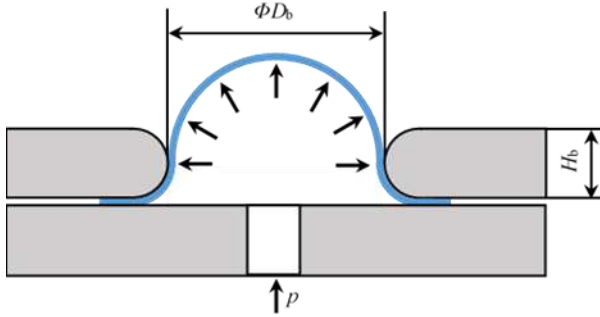


Figure 4 Bulge test diagram

### 3.3.1 The Strain of Bulge Test

The strain of the film in bulge test is usually sampled from the large deformation area near the top of the inflated balloon. While inflating, the position changes of the balloon pole and the points nearby were recorded and selected for relevant calculation, then the sphere radii were fitted and the strain calculated (Figure 5). Based on the hypothesis of spherical shape, two observation points along the longitude of the inflated sphere surface,  $P_{i-1}$  and  $P_i$ , were taken to analyze. In the figure,  $P_0$  refer to the pole, which is also the center of the disc diaphragm in undeformed state;  $\theta_i$  and  $\Delta\theta_i$  are the central angle corresponding to the arc  $\widehat{P_0P_i}$  and  $\widehat{P_{i-1}P_i}$  respectively;  $h_{i-1}$ 、 $h_i$  are the inflated height of the points,  $r_{i-1}$ 、 $r_i$  the distances from the axis of symmetry. Hence, the longitudinal and latitudinal stretch ratios at the point  $P_i$  can be calculated:

$$\lambda_1 = \frac{\widehat{P_{i-1}P_i}}{\Delta L} = \frac{R_i \Delta\theta_i}{\Delta r_i^0} \quad (14)$$

$$\lambda_2 = \frac{r_i}{r_i^0} \quad (15)$$

where  $R_i$  is the curvature radius at the point  $P_i$ ;  $\Delta r_i^0$  is the distance between the points in undeformed state,  $r_i^0$  is the distance from the center to  $P_i$ .

According to the above assumptions and the geometric relationship shown in the Figure 5, there also are

$$\frac{\Delta\theta_i}{2} = \tan^{-1} \frac{\Delta L}{2L_P} \quad (16)$$

$$R_i = \frac{\Delta L}{2} / \sin^{-1} \frac{\Delta\theta_i}{2} \quad (17)$$

where  $L_P$  is the chord distance to the sphere center,  $\Delta L$  the chord length.

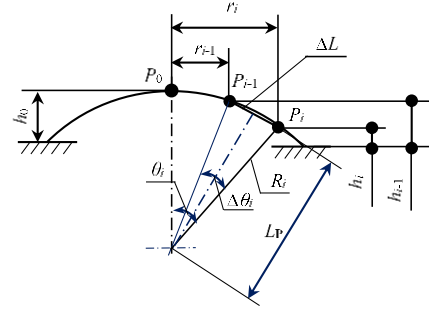


Figure 5 Geometry calculation of a spherical cap

When the distance between two observation points is small enough, the equation can be used to approximate the curvature radius of the surface points of the inflated sphere; When the starting point of chord is fixed to the pole, the obtained  $R_i$  is the average radius, i.e., the "inflated sphere" is considered as standard. Therefore, by measuring the vertical and horizontal displacement of the observation points along the longitude, the stretch ratios of the inflated film can be calculated, and the deformation can be analyzed.

### 3.3.2 The Stress of Bulge Test

Assuming that the inflation shape in bulge test is spherical and its radius of curvature  $R$ , the longitudinal and latitudinal stretch ratios are equal, i.e.,  $\lambda_1 = \lambda_2 = \lambda$ . According to force analysis, the equibiaxial tensile stress  $\sigma$  can be calculated [17]:

$$\sigma = pR/2t = pR\lambda^2/2t_0 \quad (18)$$

where  $p$  is the hydraulic oil (or compressed air) pressure.

## 4 Simulation Analysis of Typical Equibiaxial Tension Tests

The finite element simulation software ABAQUS can be used to evaluate whether the three typical equibiaxial tension methods are in good agreement with the theoretical calculation, or the influence of test apparatus and specimen parameters on the test accuracy.

### 4.1 Simulation of Equibiaxial Planar Tension

The simulation analysis of equibiaxial planar tension was carried out according to three cases: two-corner-point-fixed tension, single-corner-point tension and multi-point tension with two corner points fixed (Figure 6).  $\lambda^C$  was defined as the central stretch ratio calculated in the central region with

uniform deformation, and  $\lambda^o$  the external stretch ratio calculated at the tensile point, then the ratio of  $\lambda^c$  to  $\lambda^o$  becomes the tensile efficiency  $\eta^\lambda$ . For convenient comparison, all the  $\lambda^o=4.6$  were taken.

3-dimensional 8-node hybrid solid elements (C3D8H) were used to mesh the finite element model of hyperelastic film. In order to reduce the number of elements and simplify the calculation, a symmetrical 1/4 film specimen was taken for analysis. The displacement was chosen as load, and the boundary conditions were set as axis symmetry for the left vertical side and the lower horizontal side of the specimen. In the two-corner-point-fixed tension (Figure 6(a)), in order to keep the distance between the two tensile points near the corner unchanged, the tensile displacement direction of the corner points were set as  $45^\circ$  to their principal direction respectively when the loads were applied on both sides. In the single-corner-point tension, just one single corner tensile

point was set as  $45^\circ$  to horizontal (or vertical) direction (Figure 6(b)). In the multi-point tension (Figure 6(c)), the tensile points were increased based on the two-corner-point-fixed tension. Except the corner points, the other points in the equibiaxial planar tension were free from tangential.

Three strain contour maps for the different tension were shown in Figure 6. It can be seen that the large strain near the tensile points exist in the equibiaxial planar tension, and the strains are not uniform near the corner, and even there is no deformation in some areas between the two corner tensile points in the two-corner-point-fixed tension. Although increasing the tensile points in Figure 6(c), that phenomenon can not be eliminated completely. In contrast, the deformation of the single-corner-point tension (Figure 6(b)) is homogeneous in most central rectangle areas except for the small regions that close to tensile points (including corner).

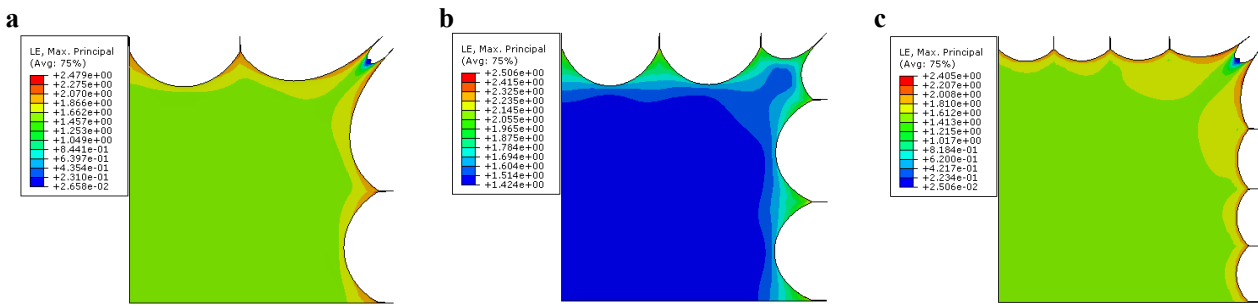


**Figure 6** Contour maps of principal strain: (a) two-corner-point-fixed tension, (b) single-corner-point tension and (c) multi-point tension with two corner points fixed.

#### 4.1.1 Analysis of the Axial Strain

The uniformity of axial deformation in the principal direction of equibiaxial planar tension determines the accuracy of the sampled strain and the value of the tensile efficiency. A series of observation points were selected from the center of the film specimen to the boundary tensile point along the tensile direction, and the positions were expressed

with the ratio of their geometry position to the original axial overall length of the analyzed specimen ( $L_s/2$ ). Assuming that the stretch ratio,  $\lambda^c$ , of the observed point near the center of specimen is uniform and standard, the stretch ratio of the point closest to the center was taken to normalize the stretch ratios from other observation points, i.e.  $\lambda/\lambda^c$ . So, the relative axial strains in different equibiaxial planar tension can be derived in Figure 7.

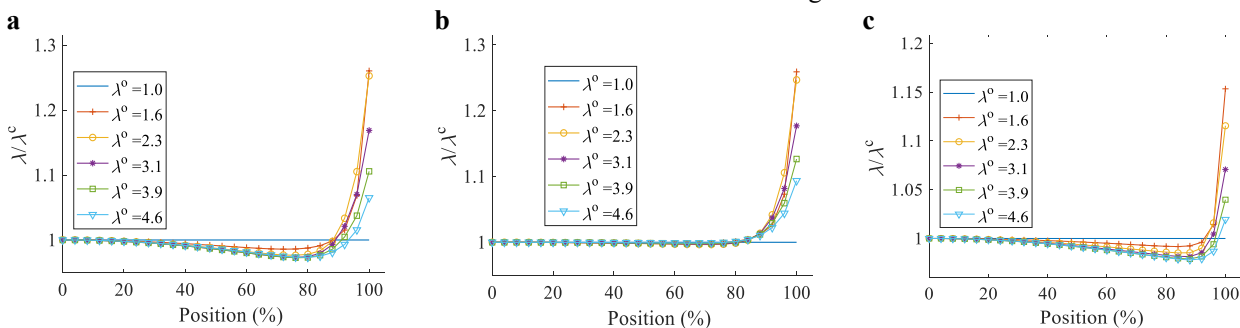


**Figure 7** The axial strains in equibiaxial planar tension: (a) two-corner-point-fixed tension, (b) single-corner-point tension and (c) multi-point tension with two corner points fixed.

It can be seen from the figure that the stretch ratios vary along the axial direction, and decreases slightly from the beginning, with the amplitude not exceeding 5%. After exceeding about 80% of the full axial length, the stretch ratios gradually increase due to the pulling of the tensile point, and reach the maximum at the tensile point. Obviously, the overall deformation of the single-corner-point tension (Figure 7(b)) is more uniform, and the strain fluctuation amplitude is not more than 1% within 80% of the full axial length; the strain fluctuation at the tensile point will decrease due to the increasing number of tensile points (Figure 7(c)). It can also be found that uniform strain can be obtained when the sampled data from less than 20% of the overall length in the two-corner-point-fixed tension (Figure 7(a), Figure 7(c)) and about 80% in the single-corner-point tension (Figure 7(b)).

#### 4.1.2 Analysis of the Stress-Strain Relationship

The tensile force at each axial tensile point was summed, and then the nominal stress could be calculated according to Eq. (12). The strain in the equation was taken from the observation point near the center of the specimen, and the stress-strain relationships of the hyperelastic film under different tension were obtained (Figure 8).

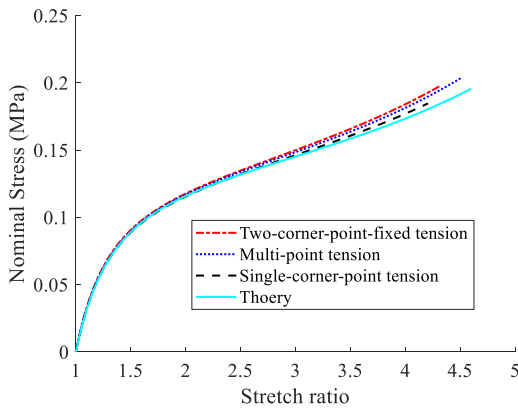


**Figure 8** Stress-strain relationships of equibiaxial planar tension

It can be seen that the mechanical properties obtained through the three typical equibiaxial planar tension methods are basically consistent with the theoretical calculation, and the discrepancy increase slightly with the stretch ratio owing to the distortion. Among them, the stress-strain simulation result of the single corner point tension is the closest to theoretical result because of uniform deformation; while the highest tensile efficiency  $\eta^\lambda$  is obtained through multi-point tension with two corner points fixed due to the increase of tensile points and the overall deformation of the specimen is more sufficient. The stress error (when  $\lambda=4$ ) and the tensile

efficiency  $\eta^\lambda$  (when  $\lambda^0=4.6$ ) calculated for three kinds of planar tension were listed in Table 2

## 4.2 Simulation of Radial Tension

In equibiaxial radial tension, the geometrical structure design of the circular specimen is key problem to ensure the test accuracy. Therefore, the circular specimen with different number of cuts and different diameters of inflation holes were modeled and analyze with ABAQUS. The specimens with the same outline dimension and equal punched hole diameter, but with 12, 16 and 24 cuts respectively, were firstly selected for modeling. 3-dimensional 8-node hybrid solid elements (C3D8H) were used to mesh the finite element analysis models. Similarly, in order to reduce the number of elements and simplify the calculation, a symmetrical 1/4 film specimen was taken for analysis, the boundary conditions were also set as axis symmetry. The grips were simulated with the circular areas between the cuts close to the outer edge of the specimen [4, 14], and the uniform radial displacements were applied to each grip. The stretch ratio  $\lambda^0$  calculated according to gripping location was 4.5.

**Table 2** Characteristics of equibiaxial planar tension

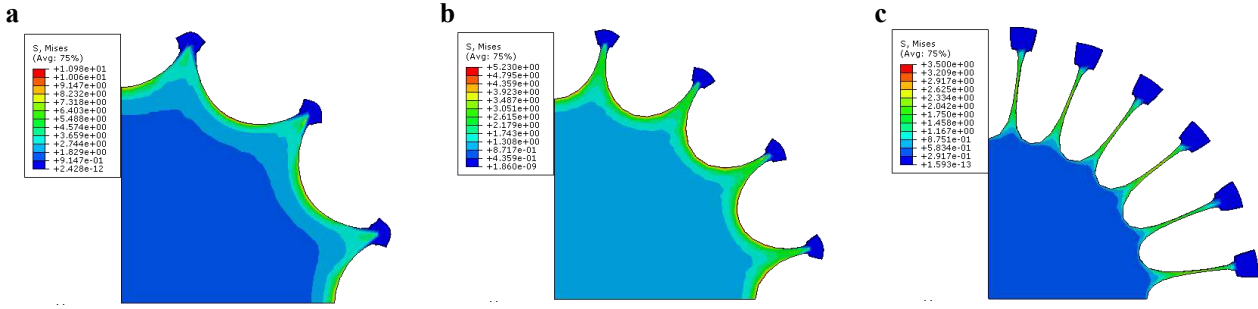
Tension method	Two-corner-point-fixed	Single-corner-point	Multi-point
Stress error (%)	6.2	2.1	4.6
$\eta^\lambda$ (%)	93.9	91.4	98.1

Figure 9 shows the Mises stress contour maps obtained by radial tension simulation of three kinds of specimens. It can be seen from the figures that the stress distribution in most areas around the center of the circular film is uniform. The maximum stress occurs along the transition arcs between the grips. Among them, the stress of 12-cut specimen is the largest and that of 24-cut the minimum. Obviously, the larger stress along the specimen transition arc between the grips is caused by larger strain due to the less cuts. However, too many cuts will lead to excessive stress on the tensile belt formed between the cuts and produce excessive deformation, which will easily lead to the material strength failure of the film specimen and decrease the tensile efficiency. Therefore, the number of cuts should be considered comprehensively between accuracy and strength.

#### 4.2.1 Principal Strain in Radial Tension

In order to further study the uniformity of principal strain in radial tension, a series of observation points were selected uniformly from the center of the circular film to the circle  $D_i$ , which is tangent to the punched hole. As with the

previous tension method, the position of each point was expressed as a percentage of the overall observation length ( $D/2$ ).



**Figure 9** Mises stress under equibiaxial radial tension: (a) 12-cut, (b) 16-cut and (c) 24-cut.

The strain calculated from each point was normalized according to the strain from the point closest to center ( $\lambda/\lambda^c$ ). The results were shown in Figure 10. It can be seen that the most stretch ratios are uniform in the principal direction, especially in the specimen with 16-cut (Figure 10(b)). From the center outwards, the strain increase slightly from the beginning, but the amplitude is very small, not more than 0.5%, and then decrease sharply. In contrast to the strain changes caused by the planar tension of the rectangular film,

the sampling points were taken in the direction of the symmetrical axis between the two grips, so the shrinkage in the stretching process led to the smaller strain at the outer end. With the number of cuts decreased, the shrinkage effects appear more obviously. It can be find from Figure 10 that when  $\lambda^0=4.5$ , the shrinkage in the 12-cut specimen is close to 8% (Figure 10(a)), while that of the 24-cut specimen is less than 4% (Figure 10(c)).

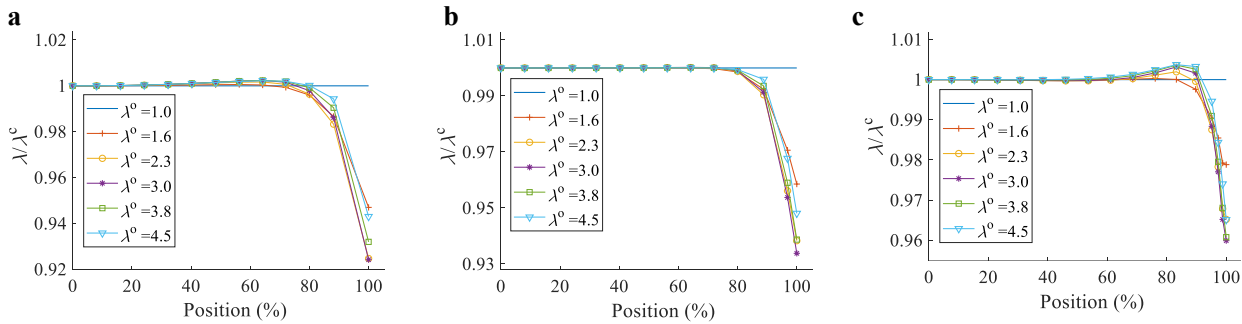


**Figure 10** Principal strain in radial tension: (a) 12-cut, (b) 16-cut and (c) 24-cut.

#### 4.2.2 Stress-Strain Relationship

Summing the tensile forces of the radial tensile points, the nominal stress could be calculated according to Eq. (13). The calculated strains were also taken from the observation point closest to the center, and the stress-strain relationships of the hyperelastic film specimens with different number of cuts were obtained (Figure 11).

It can be seen from Figure 11 that the mechanical properties of the film materials obtained by the three kind of specimens are close to the theoretical results. The more cuts the specimen are there, the more uniform the deformation of the specimen is, and the more accurate the stress-strain relationship can be gain. When  $\lambda=4$ , the stress error of 24-cut specimen is the smallest, which is less than 4% compared with the theoretical calculation result.

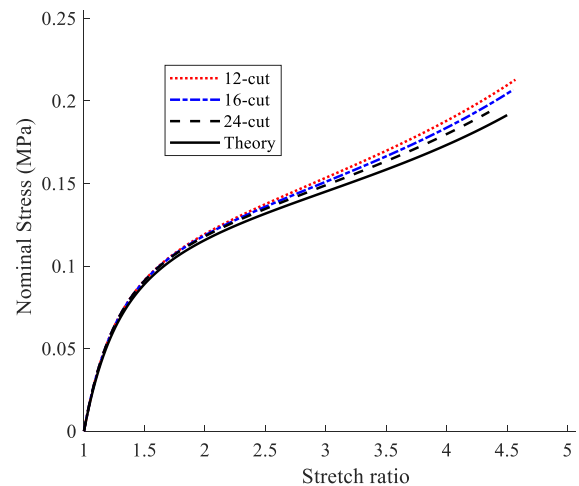


**Figure 11** Stress-strain relationships in radial tension

Due to the excessive deformation along the transition arc between the grips, the "pull" effect in the area near the center of the specimen becomes more obvious with fewer cuts, resulting in higher tensile efficiency  $\eta^\lambda$ , where the stretch ratios of 12-cut and 16-cut specimens even exceed that from the grips. The tensile efficiency  $\eta^\lambda$  ( $\lambda^\circ=4.5$ ) and the stress errors ( $\lambda=4$ ) were calculated and listed in Table 3.

**Table 3** Comparison of stress error and tensile efficiency

Specimen	12-cut	16-cut	24-cut
Stress error (%)	8.48(8.59)	6.05(8.46)	3.83(4.65)
$\eta^\lambda$ (%)	101.52(98.03)	101.12(99.55)	96.72(100.04)

Note: The data in brackets were from the punched specimens with the diameter reduced by half.

### 4.2.3 Influence of the Punched Hole

Reducing the diameter of the punched hole will increase the tensile stress along the transition arc, resulting in larger stress error, as shown in Table 3. However, reducing the diameter does not improve the tensile efficiencies in 12-cut and 16-cut specimens, which are mainly caused by the increase of the diameter ( $D_i$ ) of the deformed tangential circle at the same time. In addition, increasing the diameter of the punched hole will lead to excessively fine tensile belt between the cuts, which will lead to excessive stretching deformation and strength failure of the film material.

## 4.3 Simulation of Bulge Test

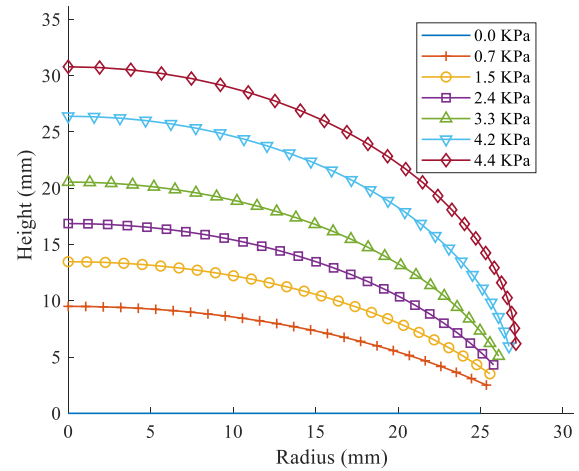
In bulge test, the deformation contour error and uniformity will affect the test accuracy. As the specimen is a circular diaphragm, the main influence factors affecting the test results should be the structure parameters of the test apparatus, including the inflation hole diameter  $D_b$  of the upper flange, the thickness  $H_b$  of the flange which also forms the transition arc radius ( $H_b/2$ ). Therefore, the simulation of bulge test mainly focused on the bulge test itself and the structure parameters of the apparatus.

In order to reduce the calculation workload, the EAP diaphragm adopted 4-node, bilinear axisymmetric quadrilateral hybrid element (CAX4H) model. The upper and lower flanges were set as discrete rigid bodies, there were no friction contact between the film and flanges during inflation, and the pressure was applied under the circular diaphragm. In the actual bulge test, in order to measure the deformation, optical device was used to measure the shape and strain of the circular marks printed on the surface of the specimen [19]. In the simulation, the positions of the center point and nearby points on the surface of the circular diaphragm were recorded during the inflation, then the spherical curvature radii calculated. Finally, the strain and

stress were derived according to the above equations.

### 4.3.1 Influence of the Profile Deformation

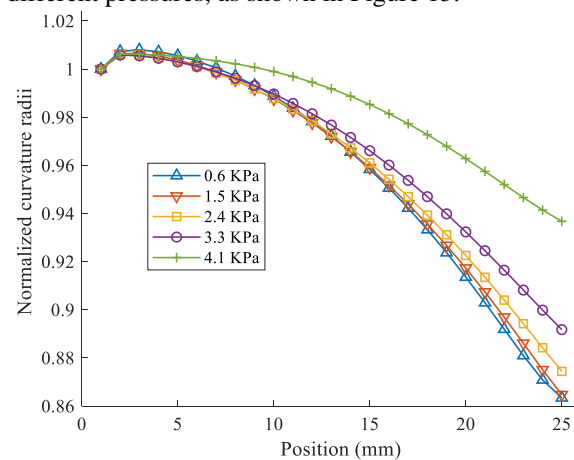
Starting from the symmetry center of the circular film, a series of observation points with equal distance (1 mm) in the undeformed state were taken to record their positions during the test, then the profile curves of the balloon can be obtained (Figure 12). It can be seen from Figure 12 that the curvature at each observation point of the spherical surface is inconsistent in the process, which is flat near the pole and steep outwards. This phenomenon is especially obvious in the initial stage.



**Figure 12** Changes of the surface profiles

#### (1) Contour error of the inflation sphere

The curvature radii were calculated by fitting the small pieces of curve between the adjacent observation points on the surface of the inflated balloon, and the curvature radii were normalized by the radius of the point closest to pole (1 mm away from the symmetry axis) to understand the contour changes of the sphere under different pressures, as shown in Figure 13.

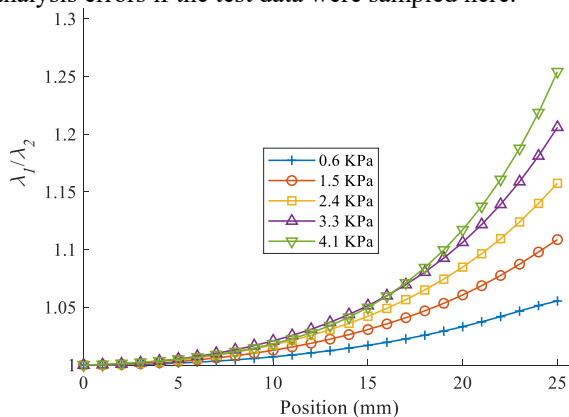


**Figure 13** Normalized curvature radii

As can be seen from the figure that when the pressure is less than 2.4 KPa, the curvature radius at the outside observation point (25mm away from the symmetry axis) is less than that at the point near the sphere pole (1 mm away from the symmetry axis) by more than 12%. With the volume increased, the difference gradually decreases. When the air pressure reached 4.1 KPa, the difference decreases to about 6.3%. It shows that the curvature radii of the profile tend to be the same and the shape becomes more spherical with the increase of the inflation pressure.

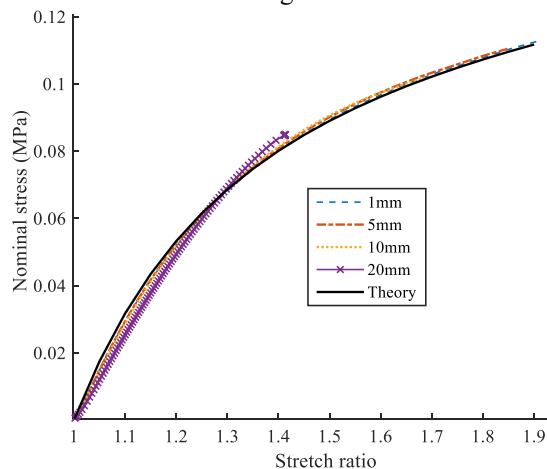
## (2) Uniformity of the deformation

In bulge test, the deformation degree of the film is uneven because the periphery clamped and fixed, where the deformation in the latitude direction close to zero. From the comparison of the longitudinal and latitudinal stretch ratios as shown in Figure 14, the longitudinal stretch ratio is larger than that of the latitudinal in the deformation process, and the closer to the clamping edge, the greater the difference is; with the increase of air pressure, this trend becomes more significant. At the remote observation point (25mm away from the axis of symmetry), when the inflation pressure reached 4.1KPa, the longitudinal stretch ratio exceeds the latitudinal stretch ratio by about 25.4%, that would result in large analysis errors if the test data were sampled here.

**Figure 14** Comparison of the longitudinal and latitudinal stretch ratios

The contour error and the non-uniform deformation of the inflation sphere will lead to the inaccuracy of the calculation results of the stress-strain characteristic curve and affect the test result. Four points with different distances in undeformed state (1 mm, 5 mm, 10 mm, 20 mm away from the center of disc diaphragm respectively) were selected for observation. The stress-strain curves were deduced and compared with the theoretical

calculation results (Figure 15). It can be seen from the figure that the farther the observation point away from the center, the greater the test error. At the same time, the effective test range is also reduced significantly at the far point. At the farthest observation point (20 mm away from the center), when the inflation pressure reached 4.1 KPa, although the calculated stress is larger than the theoretical result by 4.7%, the actual deformation is less than half of the deformation near the spherical top due to uneven deformation, which will affect the effective test range.

**Figure 15** Comparison of the stress-strain relationships at different observation points

### 4.3.2 Influence of the Structure Parameters

The structure of the bulge test apparatus is simple, and the main parameters are the thickness  $H_b$  of the upper flange and the diameter  $D_b$  of the inflation hole (Figure 4). Therefore, three models were proposed for simulation analysis:

- The original model: The structure parameters are  $H_b = 6$  mm,  $D_b = 54$  mm;
- The thick flange model: Based on the original model, the upper flange thickness of the test apparatus structure was doubled;
- The small hole model: Based on the original model, the inflation hole of the structure was reduced by half.

The stress-strain curves obtained from the above mentioned models were shown in Figure 16 and compared with the theory result. When  $\lambda = 1.9$ , the stresses in bulge test are slightly larger than that of the theoretically calculated, but not more than 2%. Within the stretch ratio, it can be concluded that the influence of the parameters of the apparatus on the test accuracy can be ignored as long as the calculated data are sampled in the uniform deformation area near the apex of the balloon.

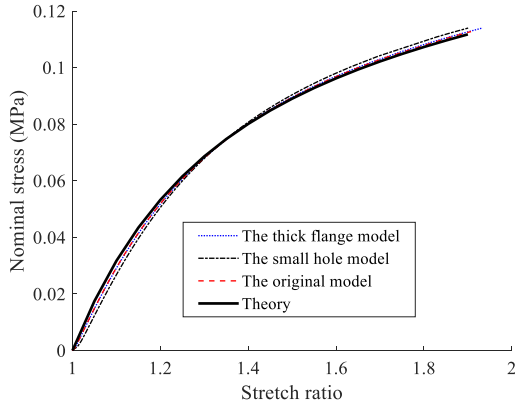


**Figure 16** Comparison of the stress-strain relationships with different structure parameters

#### 4.3.3 Influence on the Inflation Height

According to the above mentioned models for different structure parameters, the inflation height of the balloon can also be obtained (Figure 17). The figure shows that when the stretch ratio reached about  $\lambda=1.9$  at the balloon pole, the small inflation hole will reduce the volume of the inflated balloon: reducing the diameter of the inflation hole by 50%, the deformation height will be reduced by half to 17.2 mm, while the required air pressure will be doubled to about 8.83 KPa.

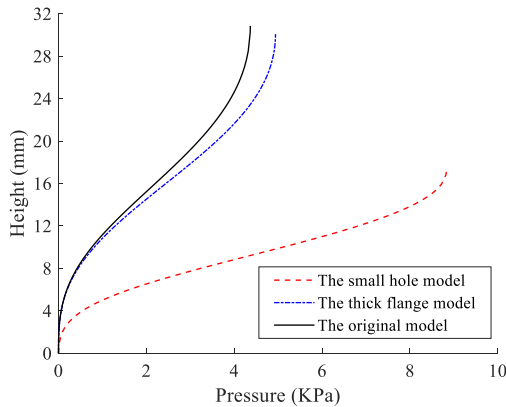


**Figure 17** Deformation in bulge tests with different structure parameters

It can be seen from Eq. (18) that the inflation pressure is inversely proportional to the curvature radius of the inflated balloon. When  $\lambda=1.9$ , the radius at the top of the balloon in the small hole model is 13.6 mm, which is about half of the radius of the original model, indicating that the deformation degree is large and then the required air pressure increased accordingly. In addition, Figure 17 also shows that thickening the upper flange will result in smaller deformation and larger required air pressure. In fact,

thickening the flange will causes the inflation hole to be smaller slightly, which is the same as reducing the inflation hole.

#### 4.3.4 Inflation Range in Bulge Test Simulation

In the above-mentioned simulation process, when the equibiaxial stretch ratio reaches about 1.9, ABAQUS reported errors, and did not converge, then the analysis quitted, resulting in the limited inflation range in bulge test simulation, which is inconsistent with the test results in practice. These problems were mainly caused by the material model and its parameters. Substituting the equibiaxial tensile stress  $\sigma$  in Eq.(10) into Eq.(18) gives

$$p = \frac{2\sigma t}{R} = \frac{4t_0(1-\lambda^{-6})}{R} \left( \frac{\partial W}{\partial I_1} + \lambda^2 \frac{\partial W}{\partial I_2} \right) \quad (19)$$

On the righthand side of Eq. (19), there are differential expression of the strain energy potential. The variable  $R$ ,  $\partial W/\partial I_1$  and  $\partial W/\partial I_2$  are the function of the equibiaxial stretch ratio  $\lambda$ , and the equation has multiple solutions to  $\lambda$  in theory. When studying large elastic deformations of isotropic materials with the strain energy potential of Mooney, Adkins [17] found that when the parameter  $\Gamma = C_{01}/C_{10} > 0.21$ , the air pressure increases monotonously with inflation; when  $\Gamma < 0.21$ , the local extreme point will appear in the pressure-deformation equation, and the extreme point of  $p$  is near  $\lambda=1.84$ . In the bulge test simulation, the maximum equibiaxial stretch ratio  $\lambda$  can be reached is about 1.90, which is close to the value in the above mentioned theoretical result.

In addition, the stress-strain values calculated by the Ogden material model parameters [9] were re-fitted to obtain the Moony-Rivlin model parameters (see Table 1). It is found that  $\Gamma=0.0038$ , which conforms to the latter condition, i.e., there are multiple deformation solutions to the pressure, leading to non-convergence in simulation analysis. Therefore, in order to increase the simulation analysis range of EAP films, the material model should be improved, and no further analysis will be made here.

## 5 Conclusions

In this paper, the finite element analysis software was used to model three typical equibiaxial tension methods, and the influences of the apparatus structure and specimen geometry parameters on the test results were also analyzed. The following conclusions were drawn:

- (1) Within a certain deformation range, the three equibiaxial planar tension methods proposed in this paper can meet the requirements of equibiaxial tension test. Among them, the deformation in the single corner

point planar tension is more uniform, and the stress-strain relationship obtained is the closest to the theoretically calculated result. Increasing the tensile points can make the overall deformation of the specimen more sufficient, thus obtaining a higher tensile efficiency  $\eta^2$ , which also helps to reduce the force error.

- (2) The main function of the cuts and punched holes in radial tension test is to avoid the specimen being torn during the test and ensure the deformation uniformity. The more the cuts are there, the more uniform the deformation is and the smaller the stress error is, but the tensile efficiency tends to decrease. The test force error can be reduced by increasing the diameter of the punched hole. However, the large hole will cause the finer tensile belt between the grips, resulting in excessive tensile deformation, and the film is prone to material strength failure. In addition, too many cuts in the specimen will make it difficult to fabricate.
- (3) In bulge test, the sampled point for calculation should be as close as possible to the pole of the sphere to obtain accurate equibiaxial stretch ratio and larger test range. The structure parameters of the test apparatus have little influence on the final test results, but the large inflation hole can reduce the required test pressure, while the small hole possesses low deformation height. In addition, the material model and its parameters will affect the range of EAP simulation analysis under certain conditions.

In a word, after taking some effective measures, the above-mentioned three equibiaxial tension methods can obtain more accurate test results and meet the requirements of equibiaxial tension test.

## 6 Declaration

### Availability of data and materials

The datasets used or analyzed during the current study are available from the corresponding author on reasonable request.

### Competing Interests

The authors declare no competing financial interests.

### Funding

Supported by Natural Science Research Projects in Jiangsu Universities of China (Grant No. 18KJA4600050), High Level Talent Project of "Six Talent Peaks" in Jiangsu Province of China (Grant No. GDZB-024), Open Project of National Key Laboratory of Robotics of China (Grant No.

2018-016), Doctoral Fund of Nanjing Vocational College of Information Technology of China (Grant No. YB20160201).

### Authors' Contributions

The author's contributions are as follows: Hua-an Luo wrote the initial manuscript; Hai-feng Zhao and Jing-jing Zhang assisted with the simulation process; Yin-long Zhu revised the manuscript. All authors read and approved the final manuscript.

### Acknowledgements

The authors sincerely thanks to Professor Hua-ming Wang of *Nanjing University of Aeronautics and Astronautics* for his constructive suggestion during manuscript preparation.

### Authors' Information

**Hua-An Luo**, born in 1968, is currently an associate professor at *Nanjing Vocational College of Information Technology, China*. He received his PhD degree from *Nanjing University of Aeronautics and Astronautics, China*, in 2015. His research interests include mechatronics engineering, intelligent material, flexible actuator. Tel: +86-25-85842324; E-mail: luoha@njcit.cn

**Yin-Long Zhu**, born in 1981, is currently an associate professor at *Nanjing Forestry University, China*. He received his PhD degree from *Nanjing University of Aeronautics and Astronautics, China*, in 2012. His research interests include mechatronics engineering, intelligent material, flexible robot. Tel: +86-25-85427751; E-mail: ylzhu@njfu.edu.cn

**Hai-Feng Zhao**, born in 1981, is currently an associate professor at *Nanjing Vocational College of Information Technology, China*. He received his PhD degree from *North University of China, China*, in 2020. His research interests include intelligent material, sensor design. Tel: +86-25-85842176; E-mail: zhaohf@njcit.cn

**Jing-Jing Zhang**, born in 1979, is currently a lecturer at *Nanjing Vocational College of Information Technology, China*. He received her master degree from *Chongqing University of Posts and Telecommunications, China*, in 2005. Her research interests include electromechanical engineering and hydraulic technology. Tel: +86-25-85842324; E-mail: zhangjj@njcit.cn

### Author Details

<sup>1</sup> School of Intelligent manufacturing, Nanjing Vocational College of Information Technology, Nanjing 210023, China

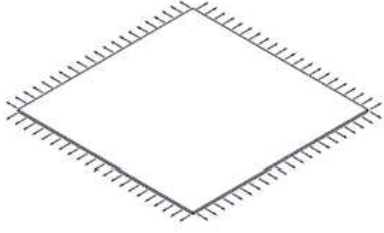
<sup>2</sup> College of Mechatronics Engineering, Nanjing Forestry University, Nanjing 210037, China

## References

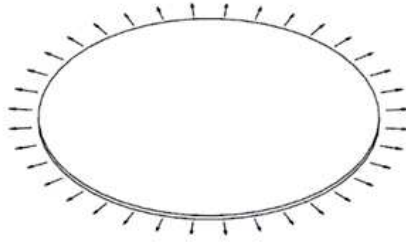
- [1] M R Mansouri, H Darijani, M Baghani. On the Correlation of FEM and Experiments for Hyperelastic Elastomers. *Experimental Mechanics*, 2017, 57(2):195-206.
- [2] Bin Fu, Xiao-Xiang Yang, Lu Wang. An Amended 8-Chain Model for Rubber-Like Materials. *Key Engineering Materials*, 2017, 744:288-294.
- [3] R Keerthiwansa, J Javořík, J Kledrowetz, et al. Hyperelastic Material Characterization: A Method of Reducing the Error of Using only Uniaxial Data for Fitting Mooney-Rivlin Curve. *Materials Science Forum*, 2018, 919:292-298.
- [4] J Park, Y Kim, J W Yoon, et al. Finite element modeling and durability evaluation for rubber pad forming process. *IOP Conference Series Materials Science and Engineering*, 2019, 651:012096.
- [5] Y Lanir, Y.C Fung. Two-dimensional mechanical properties of rabbit skin-I. Experimental system. *Journal of Biomechanics*, 1974, 7(1):29-34.
- [6] M Zemánek, J Burša, M Děták. Biaxial tension tests with soft tissues of arterial wall. *Engineering Mechanics*, 2009, 16(1):3-11.
- [7] K Genovese, L Lamberti, C Pappalettere. Mechanical characterization of hyperelastic materials with fringe projection and optimization techniques. *Optics & Lasers in Engineering*, 2006, 44(5):423-442.
- [8] L Chevalier, Y Marco. Tools for multiaxial validation of behavior laws chosen for modeling hyperelasticity of rubber-like materials. *Polymer Engineering & Science*, 2010, 42(2).
- [9] J W Fox. An experimental study on the dynamic response of dielectric elastomer membranes. *Electroactive Polymer Actuators & Devices. Electroactive Polymer Actuators and Devices (EAPAD)*, 2007.
- [10] H A Luo, H M Wang, Y P You. Experimental Methods of Equiaxial Tension of Hyperelastic Membrane and Corresponding Simulations. *Journal of South China University of Technology (Natural Science Edition)*, 2011, 39(4):56-61.
- [11] Obata Yutaka, Kawabata Sueo, Kawai Hiromichi. Mechanical properties of natural rubber vulcanizates in finite deformation. *Journal of Polymer Science: PART A-2*, 1970, 8(6): 903-919.
- [12] Blatz, J Paul. Application of Finite Elastic Theory to the Deformation of Rubbery Materials. *Journal of Rheology*, 1962, 6(1):223-252.
- [13] N T Jacobs, D H Cortes, E J Vresilovic, et al. Biaxial Tension of Fibrous Tissue: Using Finite Element Methods to Address Experimental Challenges Arising From Boundary Conditions and Anisotropy. *Journal of Biomechanical Engineering*, 2013, 135(2):021004.
- [14] K Miller. Testing elastomer for hyperelastic material models in finite element analysis. *Axel Products Testing and Analysis Report*, 2000.
- [15] L R G Treloar. Strains in an inflated rubber sheet and the mechanism of bursting, *Transactions of the Institution of the Rubber Industry*, 1944, 19(6): 201-212.
- [16] R S Rivlin, D W Saunders. Large Elastic Deformations of Isotropic Materials. VII. Experiments on the Deformation of Rubber. *Philosophical Transactions of the Royal Society of London. Series A, Mathematical and Physical Sciences*, 1951, 243(865):251-288.
- [17] J E Adkins, R S Rivlin. Large Elastic Deformations of Isotropic Materials. IX. The Deformation of Thin Shells. *Philosophical Transactions of the Royal Society A Mathematical Physical & Engineering Science*, 1952, 244(888):505-531.
- [18] L J Hart-Smith, J D C Crisp. Large Elastic Deformations of Thin Rubber Membranes. *International Journal of Engineering Science*, 1967, 5(1):1-24.
- [19] M Sasso, G Palmieri, G Chiappini, et al. Characterization of hyperelastic rubber-like materials by biaxial and uniaxial stretching tests based on optical methods. *Polymer Testing*, 2008, 27(8): 995-1004.
- [20] T Li, Z Zou, G Mao, et al. Agile and resilient insect-scale robot. *Soft Robotics*, 2018.
- [21] Y F Chen, S Xu, Z Ren, et al. Collision resilient insect-scale soft-actuated aerial robots with high agility. *IEEE Transactions on Robotics*, 2021, PP(99):1-13.
- [22] Y L Zhu, C Hua, X F Su, et al. Investigation on flexible pressure sensor array and signal acquisition system. *Transactions of the Chinese Society of Agricultural Machinery*, 2020,51(08): 400-405+413.
- [23] S Son, N C Goulbourne, et al. Large strain analysis of a soft polymer electromechanical sensor coupled to an arterial segment. *Journal of Intelligent Material Systems & Structures*, 2012, 23(5): 575-586.
- [24] Ying-Jie Jiang, Su-Ting Liu, Mei-Lin Zhong, et al. Optimizing energy harvesting performance of cone dielectric elastomer generator based on VHB elastomer. *Nano Energy*, 2020, 71:104606
- [25] F Carpi, D De Rossi, R Kornbluh, et al. Dielectric elastomers as electromechanical transducers: Fundamentals, materials, devices, models and applications of an emerging electroactive polymer technology. *Elsevier*, 2011.
- [26] M Mooney, A theory of large elastic deformation. *Journal of Applied Physics*, 1940, 11(9): 582-592.
- [27] R S Rivlin, A G Thomas. Large elastic deformations of isotropic materials. VIII. Strain distribution around a hole in a sheet. *Philosophical Transactions of the Royal Society of London. Series A, Mathematical and Physical Sciences*, 1951, 243(865): 289-298.
- [28] O H Yeoh, Characterization of Elastic Properties of Carbon-Black-Filled Rubber Vulcanizates. *Rubber Chemistry and Technology*, 2012, 63(5):792-805.
- [29] R W Ogden. Large deformation isotropic elasticity-on the correlation of theory and experiment for incompressible rubberlike solids. *Proceedings of the Royal Society of London*, 1972, A326: 565-584.

# Figures

a



b



c

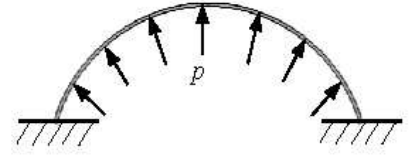
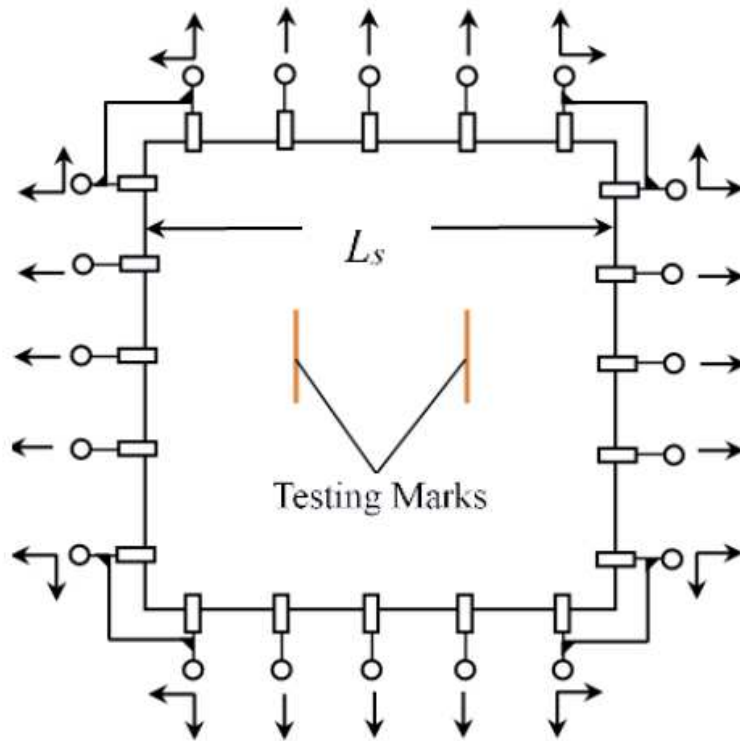


**Figure 1**

Typical equibiaxial tension test: (a) Equibiaxial planar tension, (b) Radial tension and (c) Bulge test

**a**



**b**

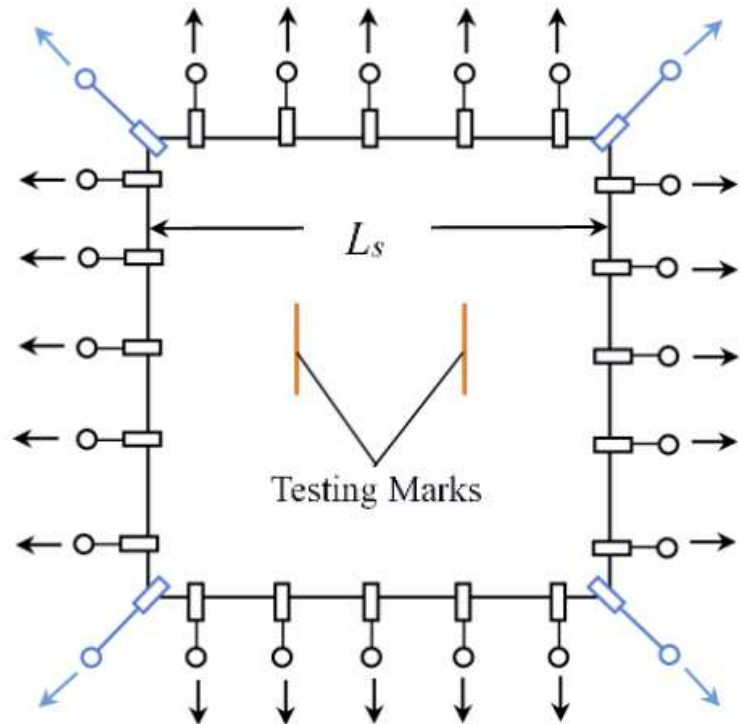


**Figure 2**

Equibiaxial planar tension test: (a) two-corner-point-fixed tension and (b) single-corner-point tension

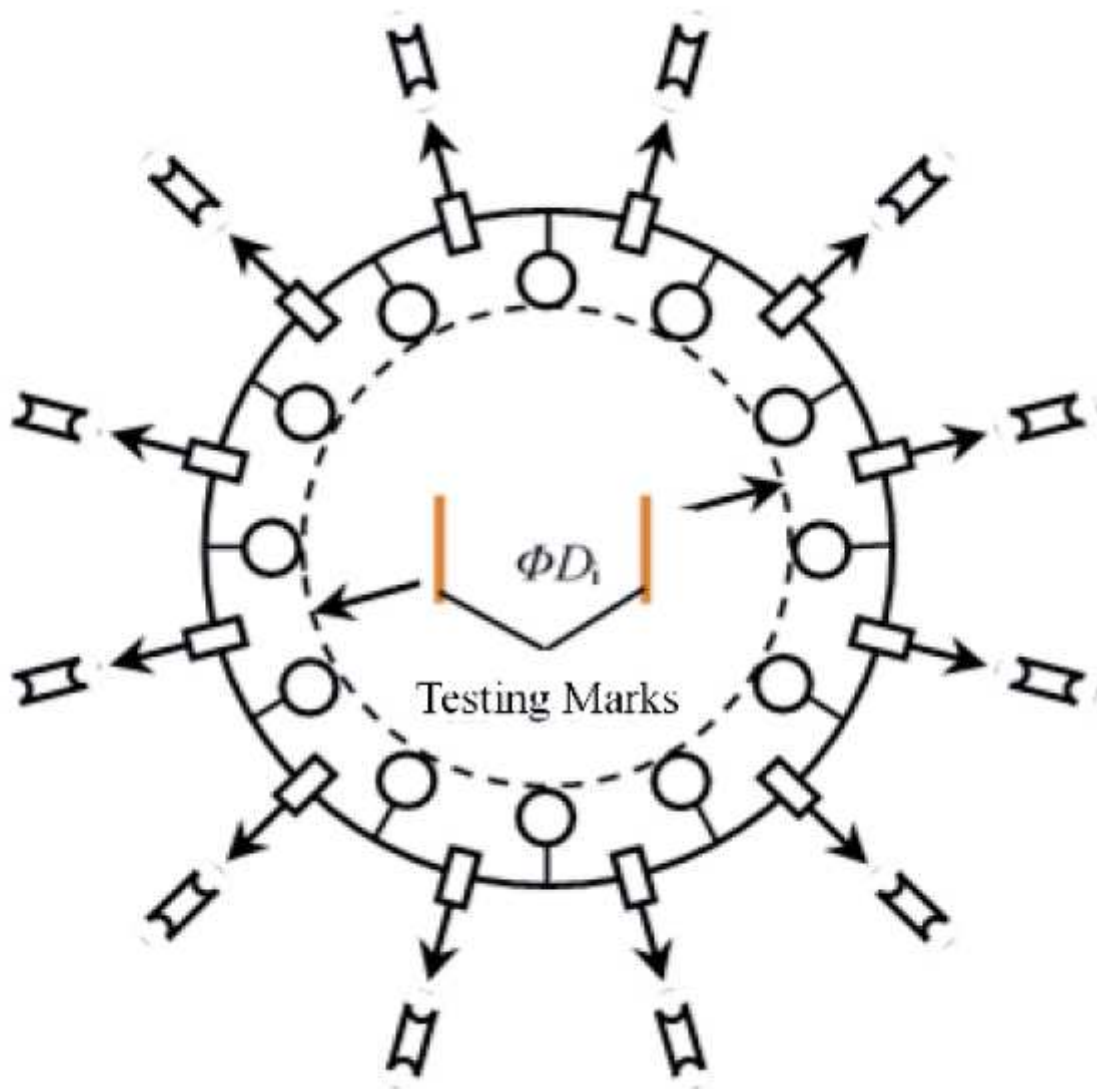


Figure 3

Radial tension diagram

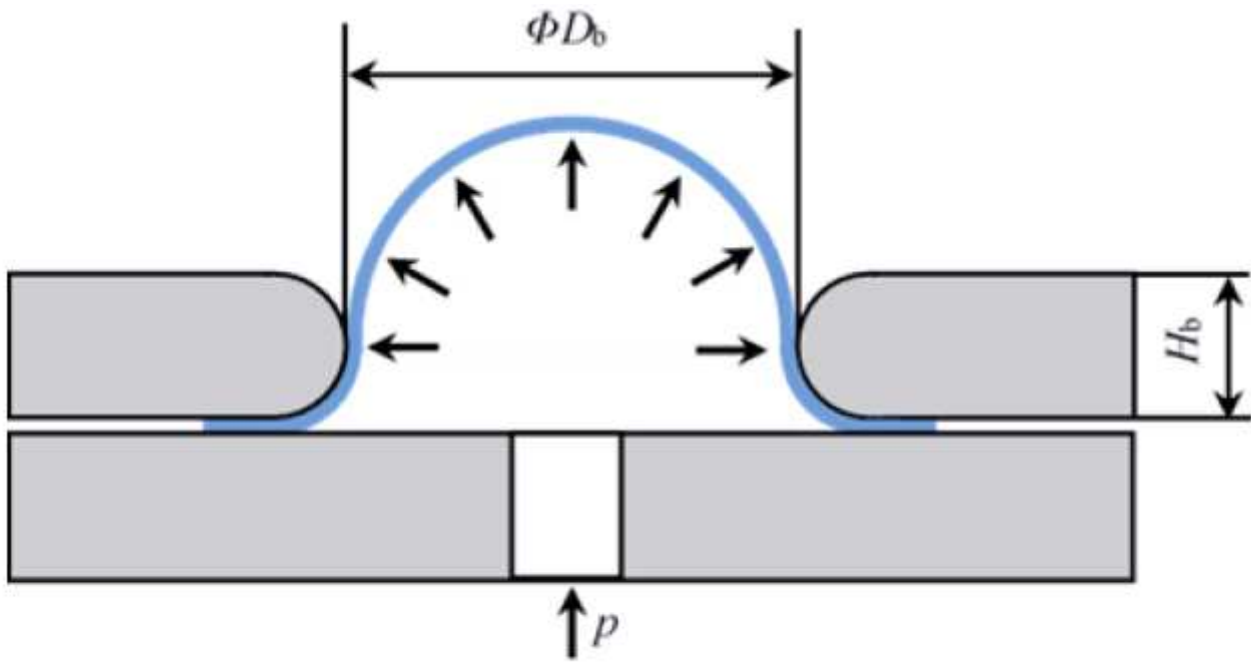


Figure 4

Bulge test diagram

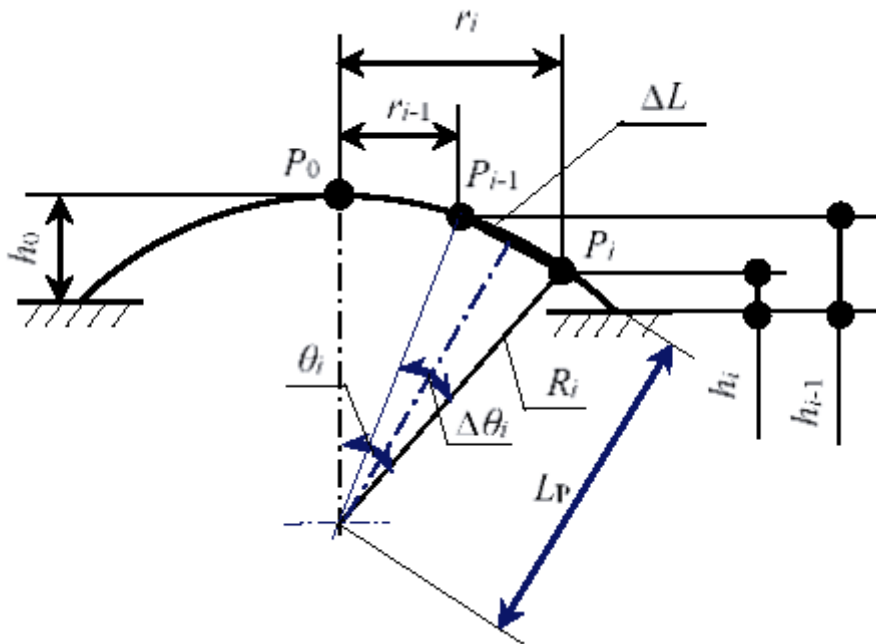


Figure 5

Geometry calculation of a spherical cap.

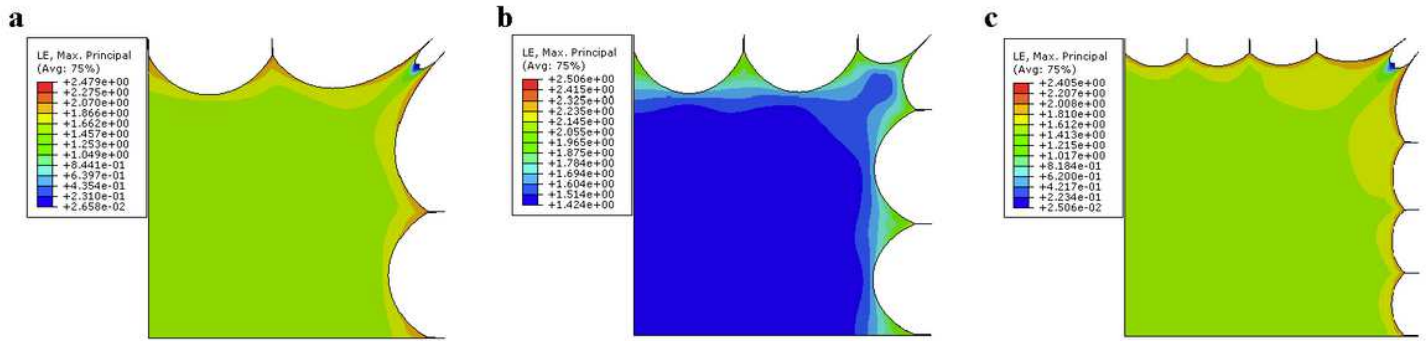


Figure 6

Contour maps of principal strain: (a) two-corner-point-fixed tension, (b) single-corner-point tension and (c) multi-point tension with two corner points fixed.

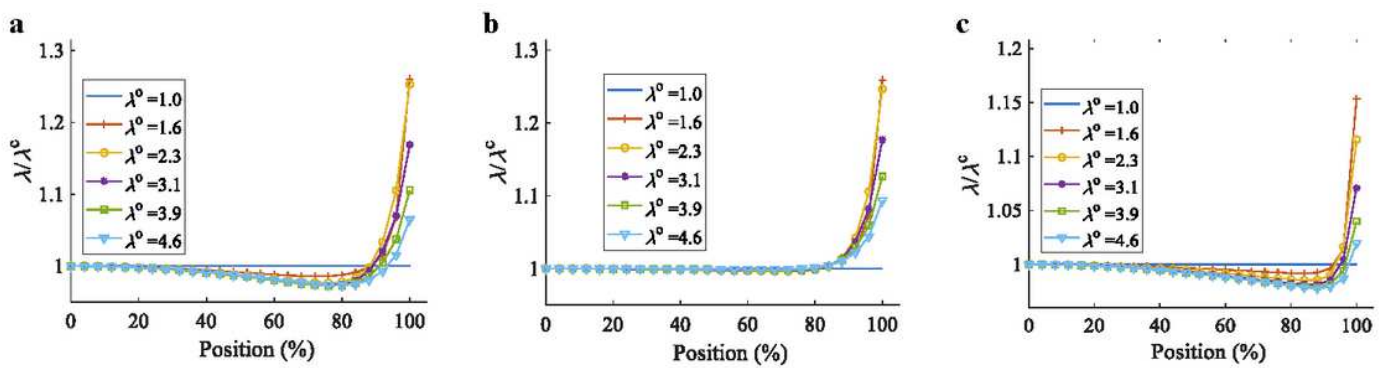


Figure 7

The axial strains in equibiaxial planar tension: (a) two-corner-point-fixed tension, (b) single-corner-point tension and (c) multi-point tension with two corner points fixed.

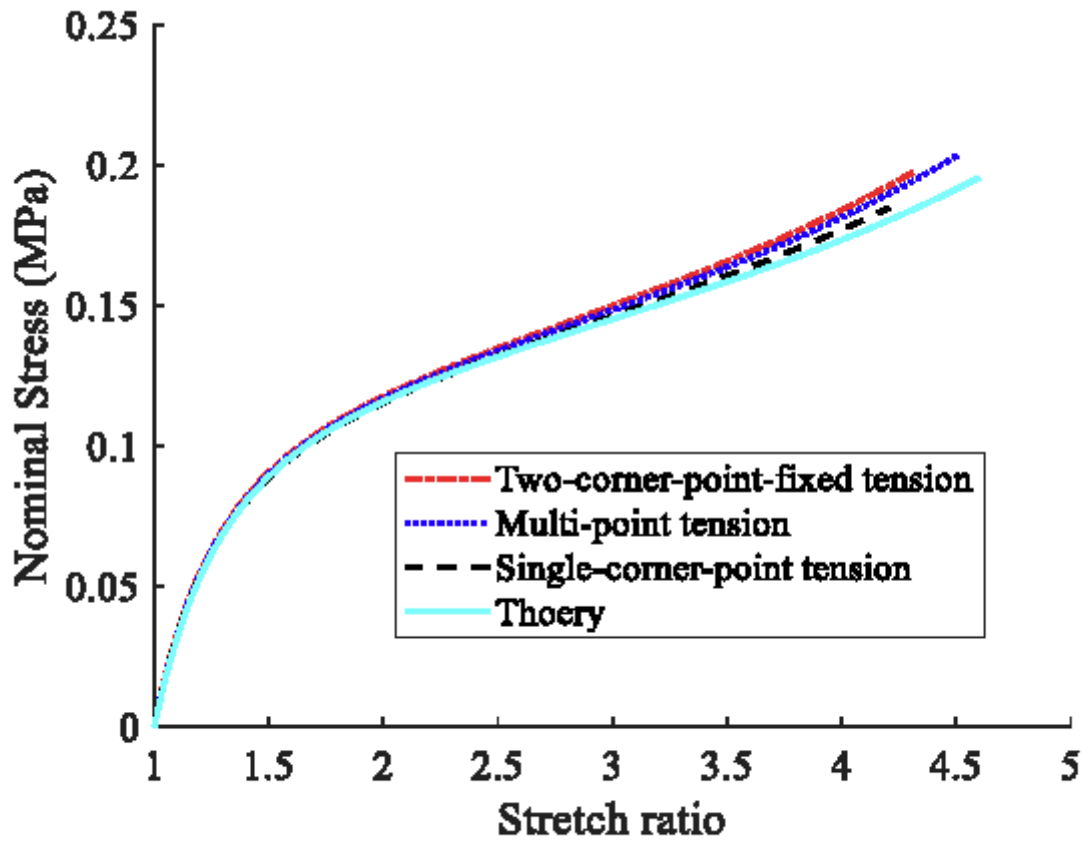


Figure 8

Stress-strain relationships of equibiaxial planar tension

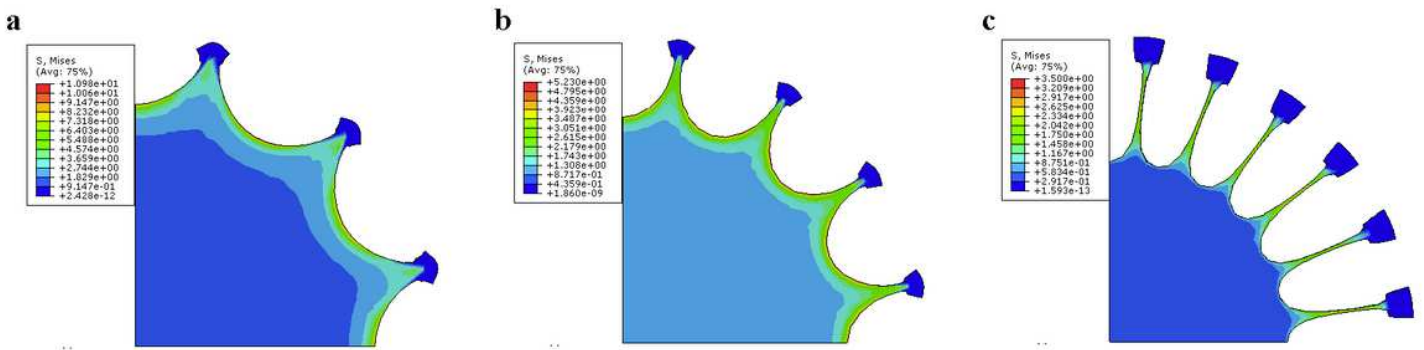


Figure 9

Mises stress under equibiaxial radial tension: (a) 12-cut, (b) 16-cut and (c) 24-cut.

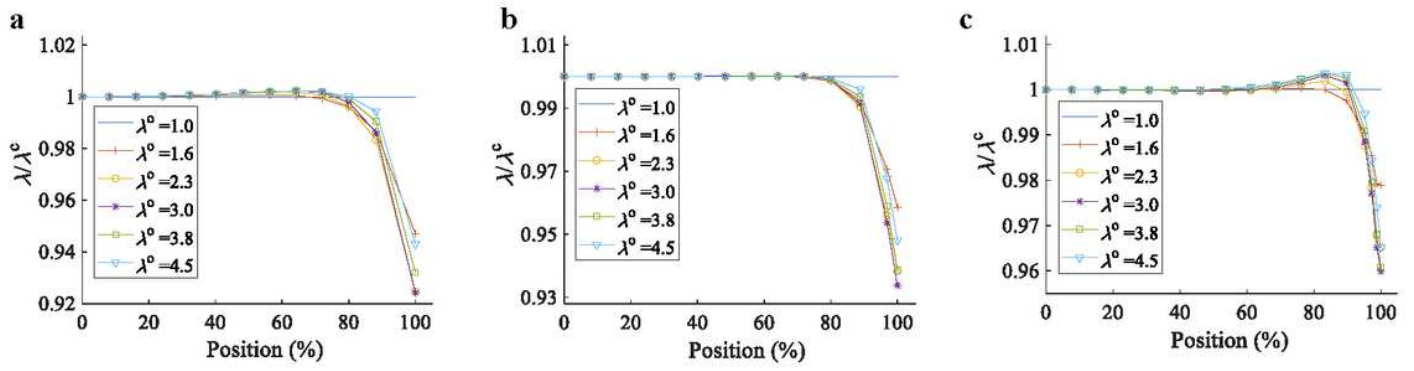


Figure 10

Principal strain in radial tension: (a) 12-cut, (b) 16-cut and (c) 24-cut.

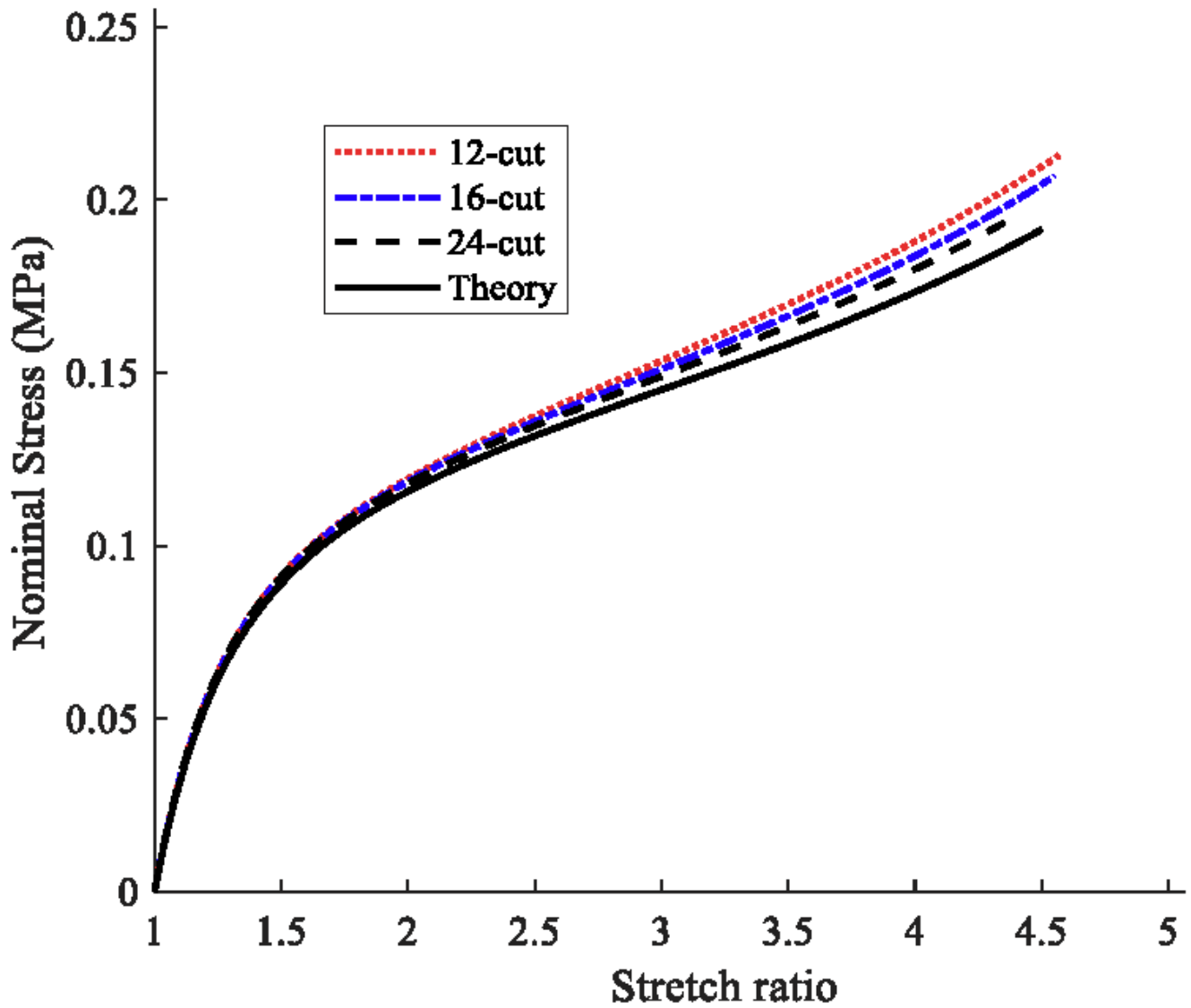


Figure 11

Stress-strain relationships in radial tension

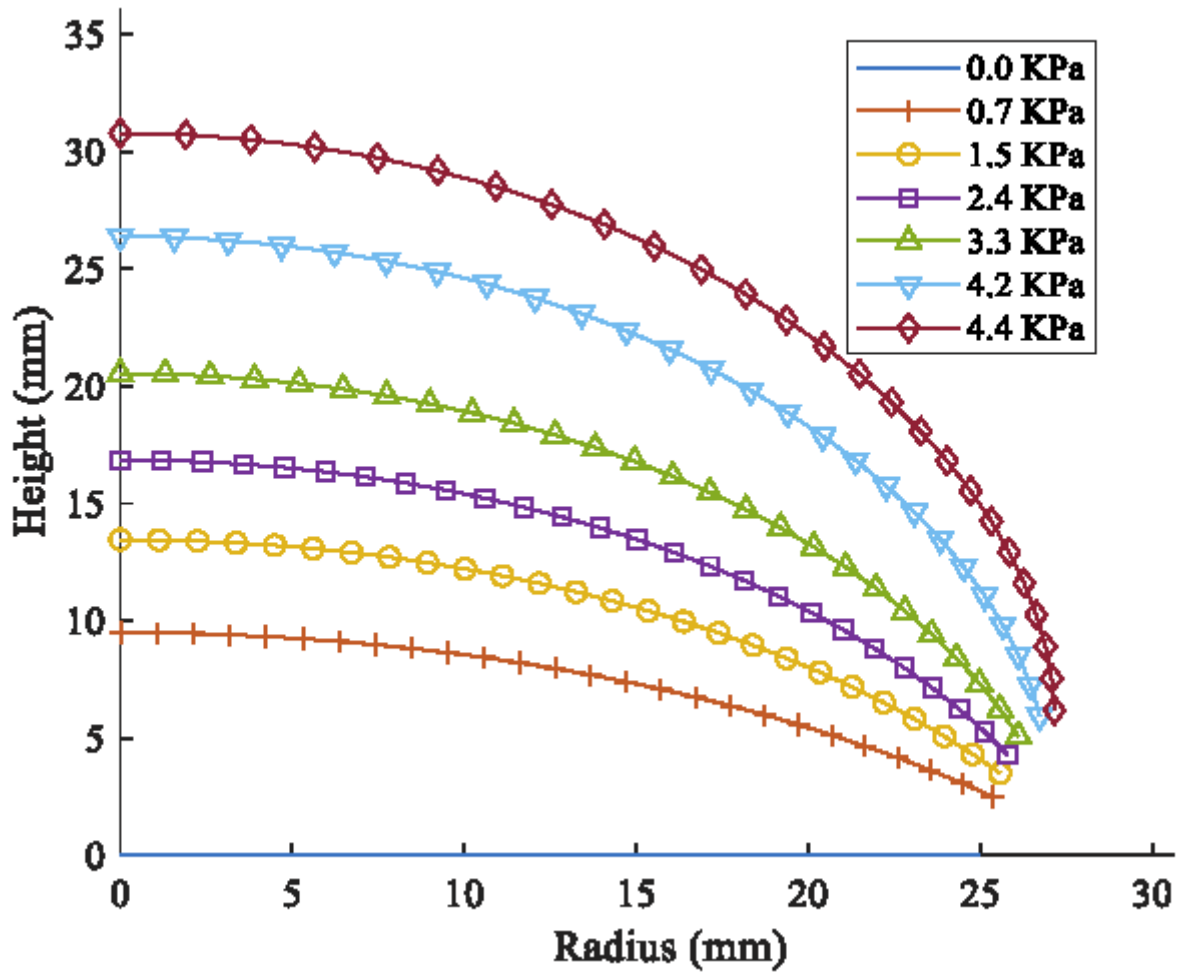


Figure 12

Changes of the surface profiles

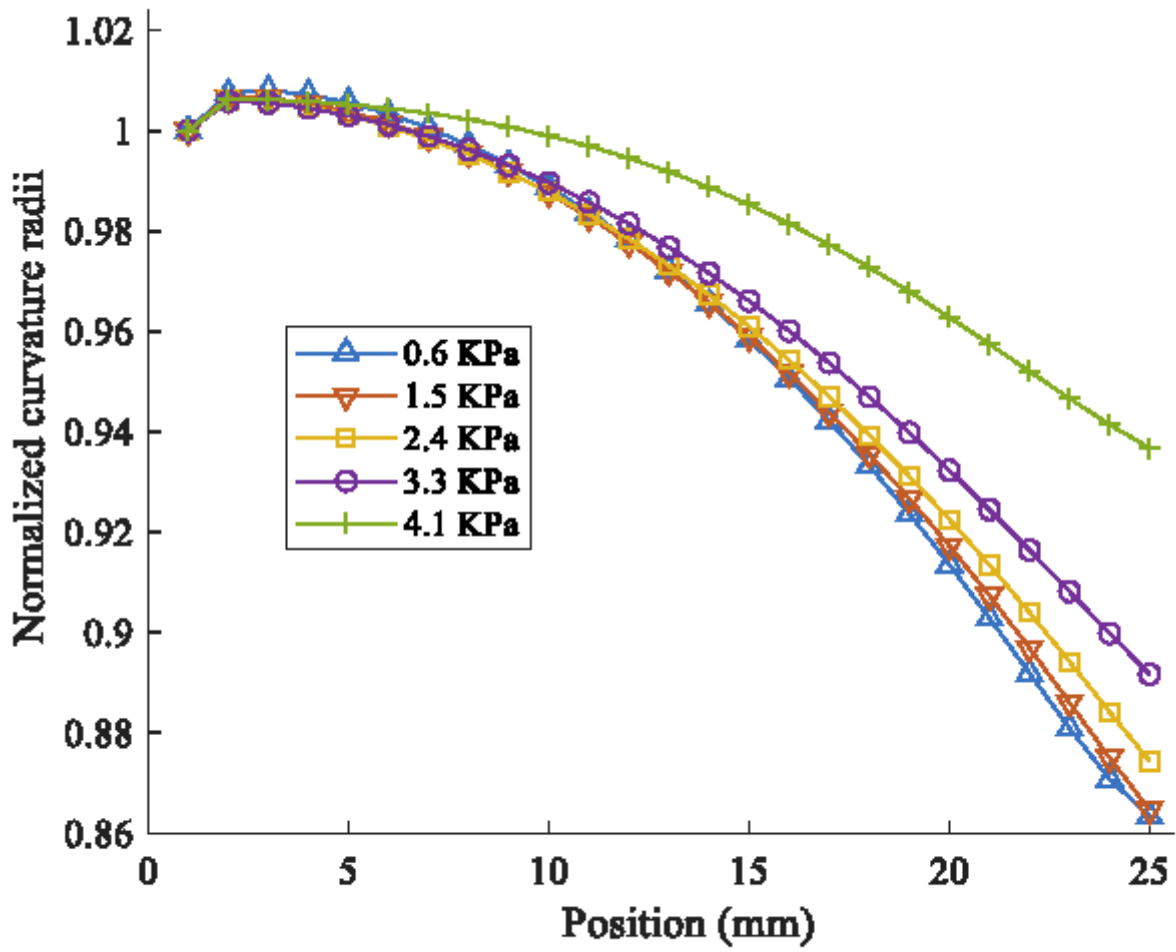


Figure 13

Normalized curvature radii

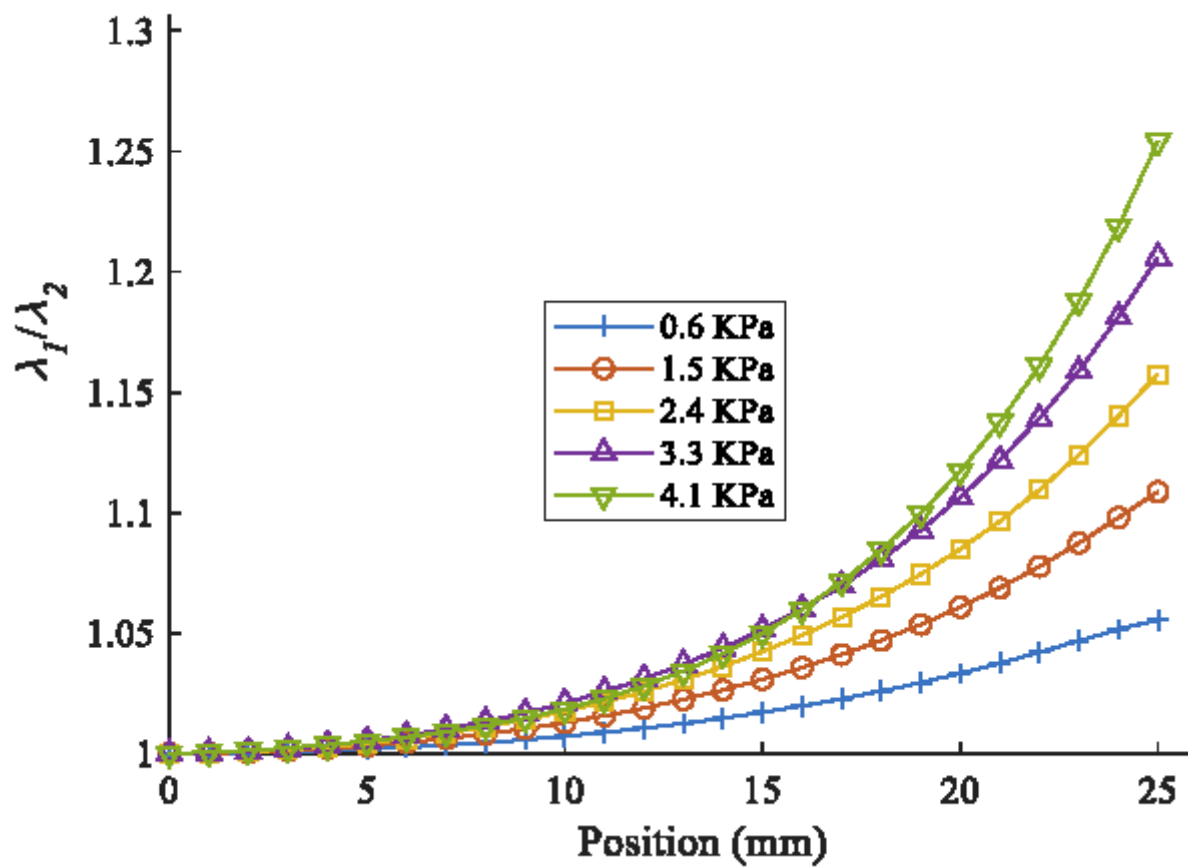


Figure 14

Comparison of the stress-strain relationships at different observation points

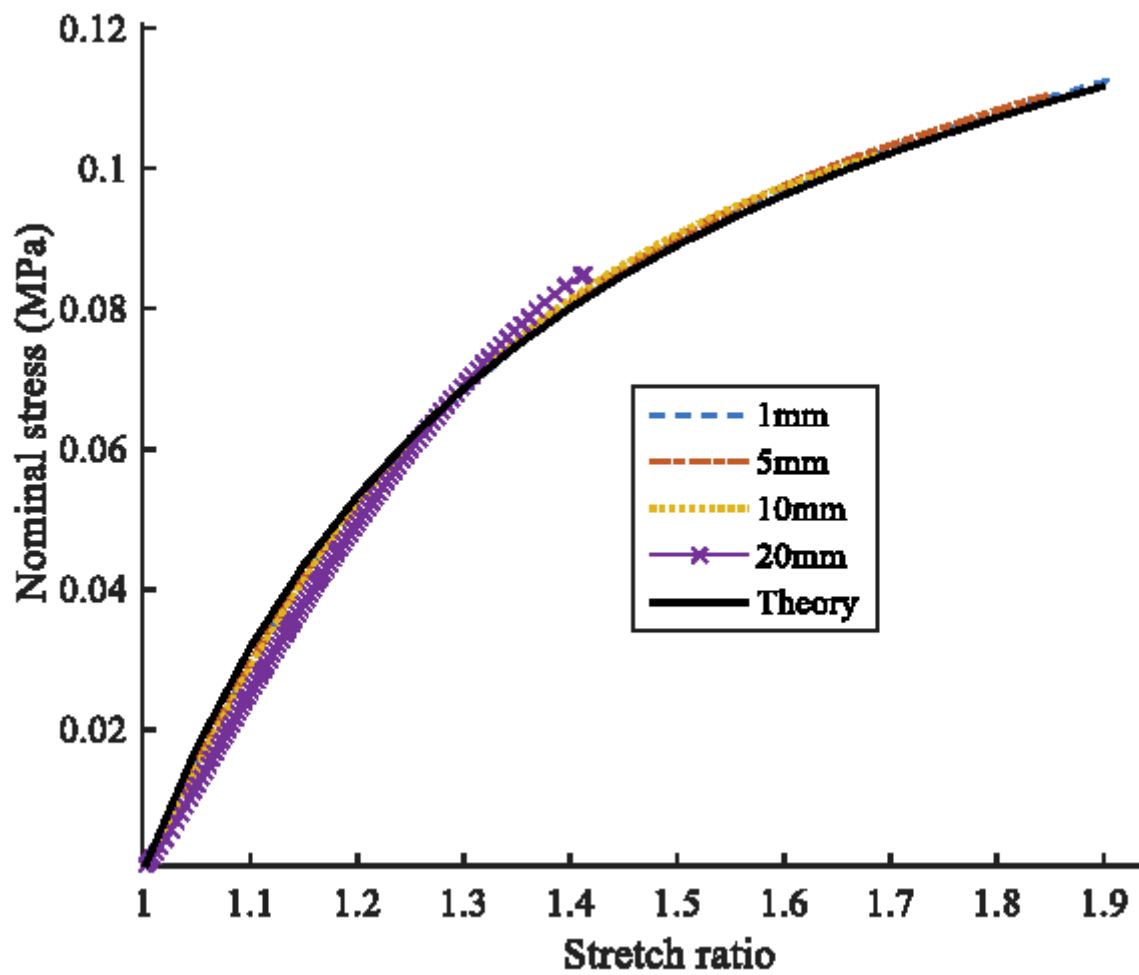


Figure 15

Comparison of the longitudinal and latitudinal stretch ratios

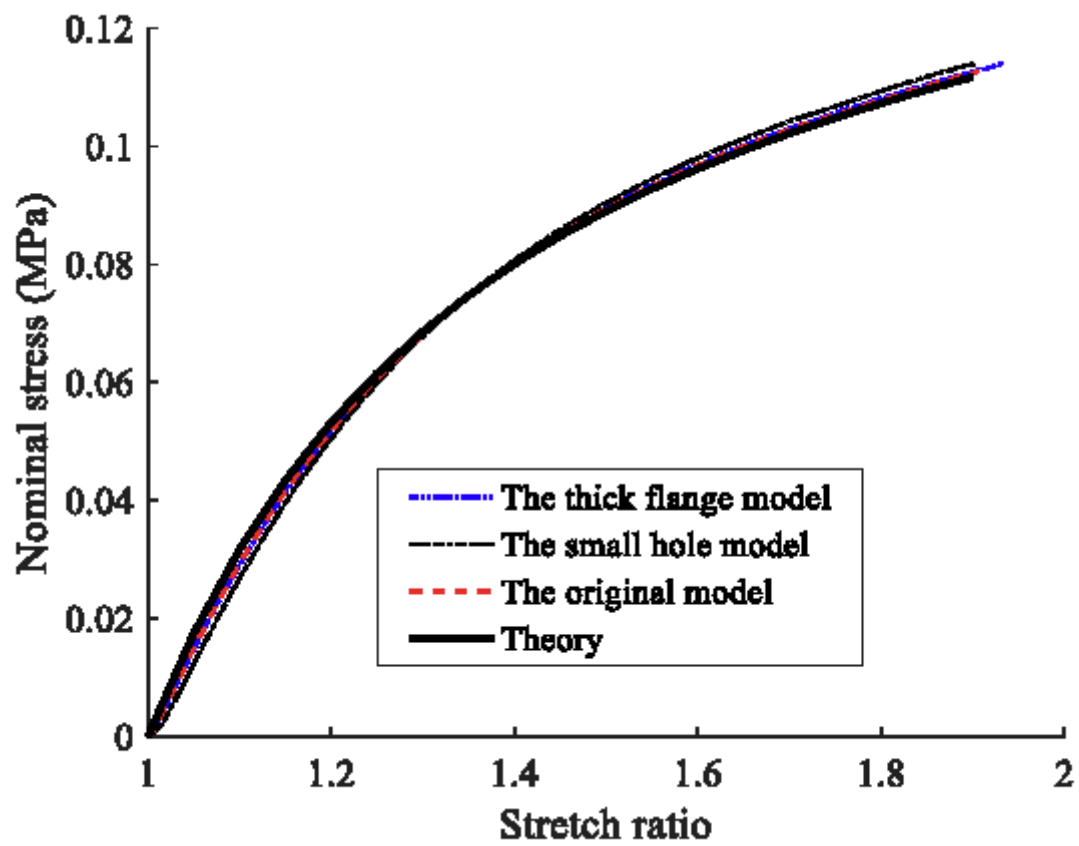


Figure 16

Comparison of the stress-strain relationships with different structure parameters

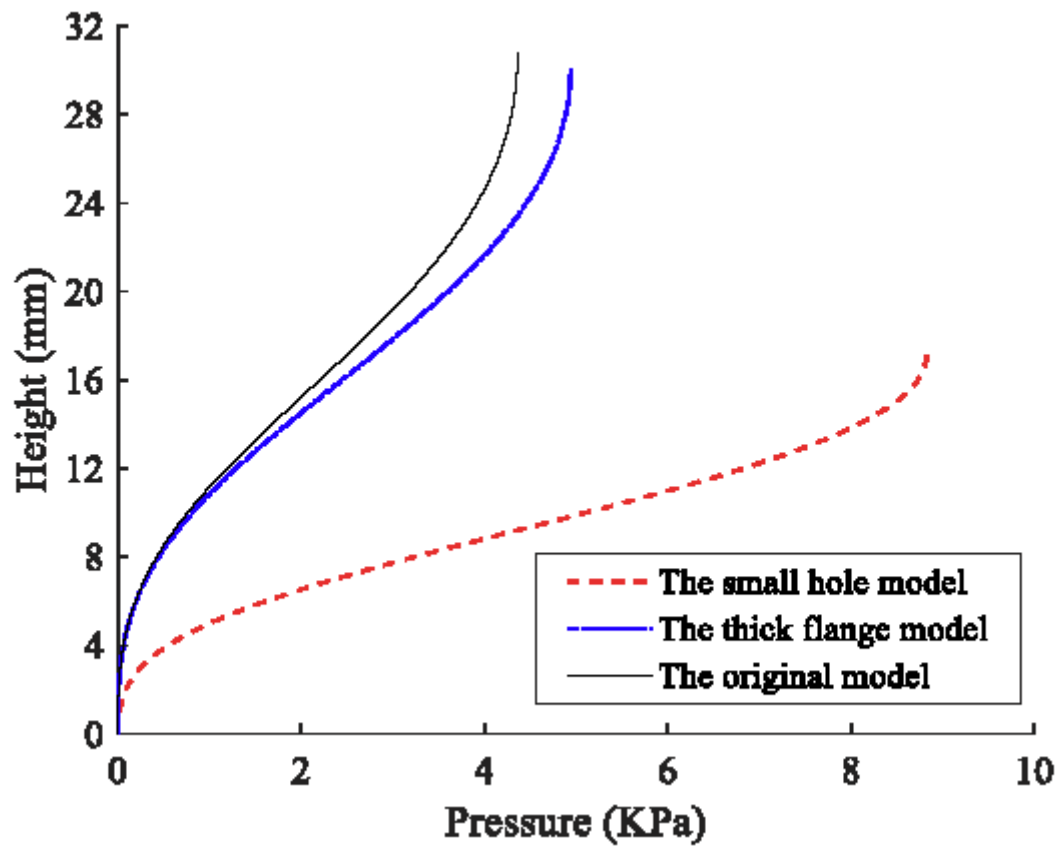


Figure 17

Deformation in bulge tests with different structure parameters